CHALMERS
UNIVERSITY OF TECHNOLOGY

High-Performance Sailing Aerodynamics

An investigation of the International Moth Class

Master's Thesis in Automotive Engineering

Philip van Hoorn

DEPARTMENT OF MECHANICS AND MARITIME SCIENCES

CHALMERS UNIVERSITY OF TECHNOLOGY
Gothenburg, Sweden 2021
www.chalmers.se

Master's thesis 2021:83

High-Performance Sailing Aerodynamics

An investigation of the International Moth Class

PHILIP VAN HOORN

Department of Mechanics and Maritime Sciences
Division of Fluid Dynamics
Chalmers University of Technology
Gothenburg, Sweden 2021

High-Performance Sailing Aerodynamics
An investigation of the International Moth Class
PHILIP VAN HOORN

Supervisor: Dr. Laura Marimon Giovannetti, SSPA
Examiner: Hua-Dong Yao, Division of Fluid Dynamics, Chalmers University of Technology

Master's Thesis 2021:83
Department of Mechanics and Maritime Sciences Division of Fluid Dynamics
Chalmers University of Technology
SE-412 96 Gothenburg
Telephone +46 31 772 1000

Typeset in LaTeX
Printed by Chalmers Reproservice
Gothenburg, Sweden 2021

Abstract

High-performance sailing is pending towards a large portion of foiling boats being sailed and built. To reach a maximum level of performance, the whole foiling boat needs to be optimised and this means optimising both hydrodynamic and aerodynamic parts. In the development of sailing classes such as the International Moth Class, the optimising of aerodynamic parts is mostly limited to trial-and-error assessments of equipment by sailors, designers, and manufacturers. There have been investigations into the stability and dynamics of the International Moth using Velocity Prediction Programs. However, these types of assessments lack the ability of seeing the influence of small design changes to the aerodynamic performance of the boat.

To asses the impact of certain design changes to the aerodynamic performance of the International Moth, a parametric Computer Aided Design (CAD) model is build, which is then used in a Computational Fluid Dynamics (CFD) investigation. A simplified model of the Moth is built. Various parameters such as sail camber, aspect ratio and wing angle can easily be adjusted to investigate the aerodynamic effects of these different parameters. Furthermore, different shapes and sizes of a “deck sweeper” are analysed, as this is a widely developed part in recent years.

The model is used to perform a parametric study of the aerodynamic performance in the CFD software STAR-CCM+. Some aerodynamic aspects that are looked at are tip vortices under the sails and endplate, as well as the optimisation of the lift to drag ratio. The CFD simulations are done for a number of apparent wind angles, to account for the effect of different parameters in different sailing conditions.

Given that the cruise speed of cars is approximately 85 km/hour (23.6 m/s) and that the average car height is nearly 2 m, it can be observed that the flows induced by cars and sails are similar, where the sails cruise at around 20 knots (10.3 m/s), and the mast height is about 6 m. The setup of the CFD investigations for these similar flow conditions would be approached in the same manner. Thus, the methodology and findings explored in the present study are generally also applicable for the aerodynamic design of cars.

Keywords: International Moth, Sailing aerodynamics, Deck sweeper, Computer Aided Design (CAD), Computational Fluid Dynamics (CFD)

Acknowledgements

I would like to thank my supervisors Hua-Dong Yao from Chalmers University of Technolgy and Dr. Laura Marimon Giovannetti from SSPA for their continuous support. Their knowledge of the subject as well as their guidance and feedback throughout the thesis were of great value.

The simulations were enabled by resources provided by the Swedish National Infrastructure for Computing (SNIC), partially funded by the Swedish Research Council through grant agreement no. 2018-05973.

I thank Frank Bramkamp at SNIC for his assistance with technical support for the simulations, which was made possible through application support provided by SNIC.

PHILIP VAN HOORN, Gothenburg, November 2021

Contents

List of Figures

List of Tables

Nomenclature

α	True wind angle
β	Apparent wind angle
ρ	Density of the fluid
τ_w	Wall shear stress
C_p	Dimensionless pressure coefficient
C_{L_A}	Drag coefficient in the apparent wind coordinates system
C_{L_A}	Lift coefficient in the apparent wind coordinates system
F_R	Driving aerodynamic force
F_T	Total aerodynamic force
F_{LAT}	Lateral aerodynamic force
M_x	Moment around the x-axis
M_y	Moment around the y-axis
M_z	Moment around the z-axis
$p_{\infty,dyn}$	Dynamic pressure in the free stream flow
$p_{\infty,stat}$	Static pressure in the free stream flow
p_{stat}	Static pressure in the point of evaluation
u	Kinematic viscosity of the fluid
u_T	Friction velocity
V_A	Apparent wind velocity
V_B	Boat velocity
V_T	True wind velocity
y	First cell thickness
y^+	Non-dimensional distance from the wall to the first mesh node
A	Surface area
AWA	Apparent wind angle
AWS	Apparent wind speed
c	Chord of the sail
CAD	Computer Aided Design
CFD	Computational Fluid Dynamics
D	Drag
EWA	Effective wind angle
IMCA	International Moth Class Association
L	Lift
TWA	True wind angle
TWS	True wind speed
VPP	Velocity Prediction Programs

1

Introduction

The International Moth class has a long history and first started out in 1928 when Len Morris built a single sail flat bottomed scow in Australia. This first iteration was 3.4 m long and had a sail area of 7.4 m^2. The outstanding performance resulted in two more similar boats being built and the Inverloch Eleven Footer class was started. The unique feature of this class was that development of the boat was permitted within a set of design parameters. Around the same time, in 1929, the American Moth Boat class was started with a very similar design to the Australian Inverloch Eleven Footer class.

In 1933 the Australians became familiar with the American Moth Boat and recognised the similar design, thus changing their class name to Moth as this rolled more easily over the tongue. In 1935 the American development class was renamed to the International Moth Class Association or IMCA. Over the years changes were made to both classes, but finally in 1972 the IMCA and the Australian Moth merged and bound by agreed upon restrictions [16].

The International Moth Class (shown in Figure 1.1) is since the year 2000 a high performance foiling sailboat. The hull is lightweight and designed for reaching "take-off" speed quickly and low drag when airborne. The foils provide the required lift to stay airborne and enable the Moth to reach top speeds of up to 36.5 *knots* (67.7 km/h) [5]. The "wings" of the Moth are designed to be light and allow the sailors to balance out the high forces resulting from the sail.

Some of the key factors of the International Moth class are stated below[13].

Key factors:

- Maximum hull length: 3.355 m
- Maximum beam: 2.250 m
- Maximum luff length: 5.185 m
- Maximum mast length: 6.250 m
- Hull weight: unrestricted (typically 10-20 kg)
- Rigged weight: unrestricted (typically <30 kg)
- Maximum sail area: 8.25 m^2
- Optimum skipper weight: 60-80 kg

Figure 1.1: Isometric view of the Mach 2.5 [12]

1.1 Motivation

As mentioned since the year 2000 the Moth is a high performance hydro-foiling boat, this also meant that the boats became more expensive and largely commercially produced. Designers such as Andrew McDougall have set the bar for optimum performance higher and higher, but the research to increase performance has mainly been trail-and-error based. Thus, an analytical approach could give interesting insight into the the various development areas of the Moth.

Over the last years the "deck sweeper" has become one of the main points of attention for further development. Two examples of used deck sweepers are shown in Figure 1.2. The different shapes of the deck sweeper could have a significant effect on the aerodynamic performance of the sail.

Furthermore, in general the research into the aerodynamic performance of small, single sail boats is limited. Thus, the results of this study might be useful for other development classes seeking increased performance.

(a) Triangular **(b)** Rectangular

Figure 1.2: Different deck sweeper panels

1.2 Aim & Methodology

High-performance sailing is pending towards a large portion of foiling boats being sailed and built. To reach a maximum level of performance, the whole foiling boat needs to be optimised and this means optimising both hydrodynamic and aerodynamic parts. In development sailing classes such as the International Moth class and the A-class catamaran, the optimising of aerodynamic parts is limited to trial-and-error assessment of equipment by sailors, designers, and manufacturers.

To give a strong scientific background to the made advances, this study for a master thesis aims to build a parametric (Computer Aided Design) CAD model of the International Moth class, which then can be used in Computational Fluid Dynamic (CFD) analyses. A simplified model will be build in the commercial program CATIA, where various parameters such as sail camber, aspect ratio and wing angle, can easily be adjusted to investigate the aerodynamic effects of these different parameters. Furthermore, different shapes and sizes of a "deck sweeper" (as shown in the figures below) will be analysed, as this is a widely developed part in recent years.

The model will be used to perform a parametric study of the aerodynamic performance in the CFD software STAR-CCM+. Some aerodynamic aspects that will be looked at are the tip vortices under the sails and endplate, as well as the optimisation of the lift to drag ratio. The CFD simulations will be done for a number of apparent wind angles, to account for the effect of different parameters in different sailing conditions.

1.3 Report Outline

Firstly, a literature study is performed in Chapter 2 to gain a solid understanding of the subject and what research has already been performed. Following, the design of the CAD model is explained in Chapter 3. Chapter 4 includes the setup of the CFD analysis, aspects such as the computation domain, the mesh and the numerical settings are described. The results from this CFD analysis are shown in Chapter 5, where the overall flow field is shown as well as a focus on certain phenomena. The main conclusions and possible future work are stated in Chapter 6.

2

Literature Study

Experimental research on the Moth

Beaver and Zsceleczky (2009) [4] performed a number of full scale measurements on a hydro-foiling Moth, with a focus on the T-foils, hydrodynamic drag of the hull and the aerodynamic forces for a hull and racks. A limited number of aerodynamic tests were performed both with and without a dummy helmsman in a tow tank facility. A typical sailing condition was chosen, with a true wind angle of 48°, true wind speed of 12 knots and a boat speed of 12 knots. This would result in an apparent wind speed of 21.9 knots, however for the tests the carriage speed was reduced to 11.88 kts (6.11 m/s) with the resulting values shown in Table 2.1. Here the force component in the course made good direction is referred to as drag and the force component perpendicular to this direction as the side force.

Table 2.1: Average measurement values from Beaver and Zsceleczky (2009) [4] (AWS = 6.11 m/s, AWA = 24°)

Helmsman	**Heel [°]**	**Drag [N]**	**Side Force [N]**
with	0	17.1	22.0
with	15.0	13.9	20.5
with	30.0	13.3	24.5
w/o	30.0	7.7	23.5

Investigations into the performance of the Moth using Velocity Prediction Programs (VPP)

A number of investigations into the dynamics and stability of the International Moth have been performed with the use of velocity prediction programs. These iterative programs generally include two mechanisms, a boat model and a solution algorithm. Different initial guesses for the input parameters need to be made and the solution algorithm tries to balance the hull and sail forces. The algorithm keeps adjusting the input parameters until a maximum possible speed is reached for a certain true wind angle. Two of these VPP investigations have been performed by Bögle (2018) [6] and Eggert (2018) [10].

Bögle used the software tool FutureShip Equilibrium (FS-Equilibrium) to evaluate the performance of Moth by stability and and force balance criteria. Input data for the windage forces were based on the aforementioned work by Beaver and Zsceleczky. The sail data was based on a combination of CFD and wind tunnel results. The CFD analysis was based on a simplified Moth sail. The predicted drag and lift coefficients used as input data for his work are shown in 2.1. Here the effective wind angle (EWA_{eff}) corresponds to the apparent wind angle while taking into account the heeling angle, as introduced by Hansen (2006) [11].

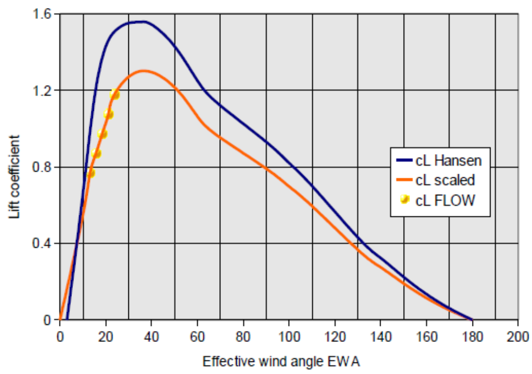

(a) Lift coefficient

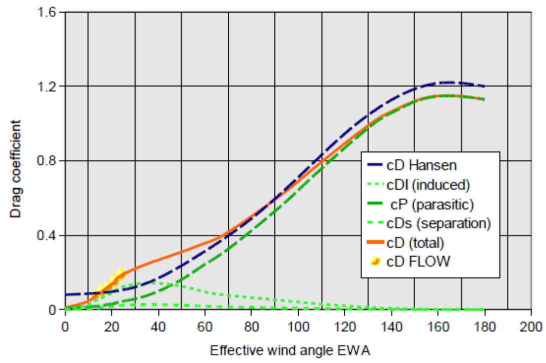

(b) Drag coefficient

Figure 2.1: Predicted lift and drag coefficients for a Moth sail from Bögle (2010) [6]

Similar initial work was performed by Eggert, who first developed a quasi static VPP model based on the same software tool FS-Equilibrium and then transformed this model into a dynamic model. The prediction of boat velocity versus true wind angles at various true wind speeds could be of interest for the purpose of this master thesis. The outcomes for the maximum velocity at up- and downwind courses were compared with the observations of an experienced sailor and active member of the Moth community Chris Williams, with the resulting values shown in Table 2.2.

Table 2.2: Predicted boat velocity (V_B) magnitude on upwind and downwind courses from Eggert (2018) [10] and Williams [18].

TWS $[m/s]$	Upwind V_B $[m/s]$		Downwind V_B $[m/s]$	
	Williams	Eggert	Williams	Eggert
5	6.5	6.7	7.3	8.9
6	7.2	7.6	8.5	10.3
7	7.7	7.4	9.6	12.2
8	7.9	7.5	10.4	13.0
9	8.0	7.5	10.8	14.2
10	8.1	7.4	11.2	14.7
11	8.2	7.2	11.7	15.9

Sailing CFD investigations

More CFD investigations have been performed on the America's Cup Class Yacht as this is one of the most prestige and well-funded sailing cups in the world. As the literature on the Moth is limited, the conclusions from this research can be of interest.

Viola (2009) [15] performed a CFD investigation into the America's Cup Class for downwind conditions and the results were compared with wind tunnel data. Mesh sizes ranging from 60000 elements up to 37 million elements were tested which showed a converging trend towards experimental values with differences below 3% for both lift and drag. However, a grid-independent solution was not achieved. Furthermore, four commonly used turbulence models, SA, SST, RLZ and k-ϵ, were tested for grid sizes of 1 and 6.5 million elements. The results showed a systematic over-estimation of the forces for all models.

Parametric sail design
The work performed by Cella et Al. (2017) [7] included the parametric design of the sail through a Python script allowing an optimization algorithm to be run together with RANS simulations. The Python scripts updated a number of variables to change the sail shape, which is subsequently used in RANS computations to maximize the velocity made good (VMG).

Fluid Structure Interaction (FSI) of a sail
The pressure from the wind deforms the sail which changes the flow characteristics over the sail. This field is called fluid-structure interaction, which commonly uses a combination of CFD and finite element methods (FEM). Bak et al. (2013) [3] performed an FSI analysis on a 30-ft yacht sail. The results showed an increase of $\approx 4.9\%$ in C_D and decrease of $\approx 1.9\%$ for C_L.

Flow around a sail
Typical flow regions around a mast and sail are described by Bailey et al. (1998) [2]:

- (I) Laminar boundary-layer flow from stagnation on the mast and windward side of the foresail.
- (IIb) Separation bubbles from the rear of the mast with turbulent reattachment on the mainsail.
- (III) Turbulent boundary-layer growth over the sail.
- (IV) Possible turbulent separation ahead of the trailing edges.

These regions are characteristic for a flow around a 2-D yacht rig and refer to Figure 2.2.

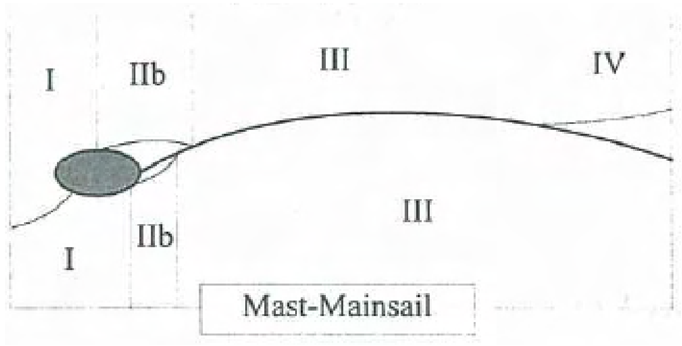

Figure 2.2: Regions around 2-D yacht rig configurations [2]

It should be noted that it is common to use so called batten cams (shown in Figure 2.3) between the mast and sail on the Moth. The smoother transition possibly reduces the separation bubble from the mast.

Figure 2.3: Mast- sail batten cam

3

CAD Model

The CAD model to be used in the simulations is based on the Moth Mach 2.5 from the company Mach 2 as shown in Figure 1.1 [12]. The model is a parametric design, such that certain aspect of the models can easily be modified. Firstly, the general model is described in Section 3.1. Then, a closer look into the design of the sail is shown in Section 3.2. And lastly, in Section 3.3 the design of different deck sweeper is discussed.

3.1 General Model

A well designed parametric CAD model is necessary to perform the CFD analysis in a good manner. The model is based on a generic Moth sailing boat, however the model is simplified in various ways as this thesis focuses only on the aerodynamics involved and not the hydrodynamics.

An isometric view of the final model is shown in Figure 3.1a. Here it can be seen that the front foil, rudder and wand are omitted as interaction with the water is not considered. Furthermore, the gantry and rigging is not included as they have a limited impact on the aerodynamics of the boat and thus would add unnecessary complexity. This results in the model consisting of four parts: the hull, the two wings and the sail as shown in Figure 3.1b.

(a) Isometric view

(b) Exploded view

Figure 3.1: CAD model

The overall dimensions of the model are shown in Figure 3.2, these dimensions represent a typical boat in the Moth class. It should should also be noted that certain parameters such as the angle of the sail and the angle of the wings can easily be altered to quickly analyse the effects of the parameters. Detailed technical drawings can be found in Appendix A.

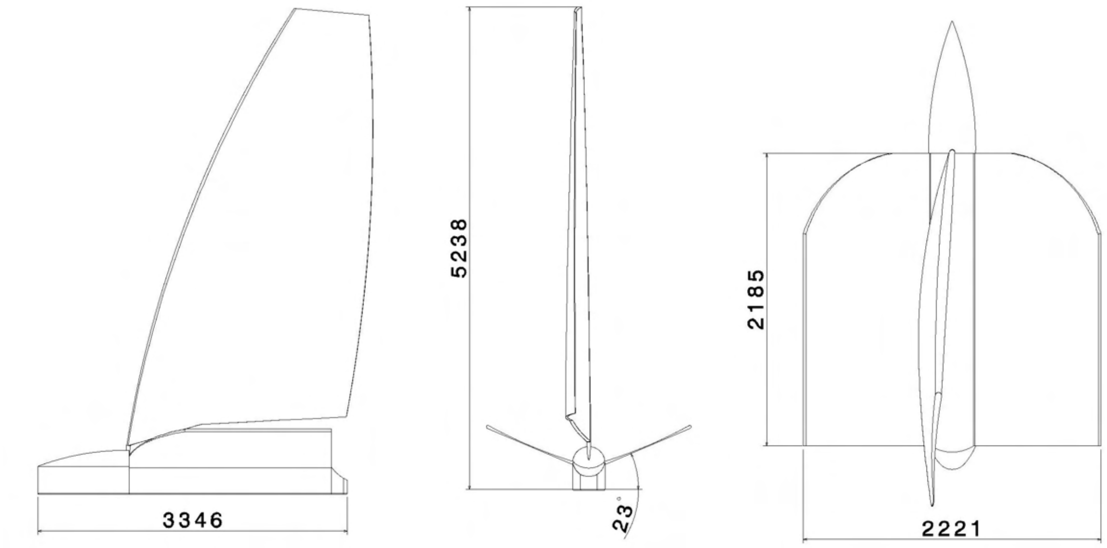

(a) Side view **(b)** Rear view **(c)** Top view

Figure 3.2: Moth model dimensions [mm]

3.2 Sail

The sail is the main component that generates the driving force of the boat and is thus very important. For the design of the sail a balance had to be found between the simplicity of the design while still representing a real sail. As mentioned previously, research showed that there is a difference in sail performance between rigid and wind pressure deformed sails. However, to include FSI of the sail would require a complex combination of CAD models, FEM, VPP and CFD. Thus, a rigid sail is assumed and it was decided to combine the mast, boom and the sail into one part, resulting in the model shown in Figure 3.3. The use of the previously mentioned batten cams would results into a similar shape as opposed to a typical mast-sail combination.

The cross-section is based on a arc with a certain radius which can be changed to alter the camber of the sail. The luff (leading edge) of the sail, representing the mast, has a diameter of 4.2 *cm* where it connects to the hull. The thickness decreases along the chord of the sail to the leach (trailing edge). The chord of the sail decreases with the height of the sail from the foot (bottom edge) to the head (top edge). Detailed technical drawings can be found in Appendix A.

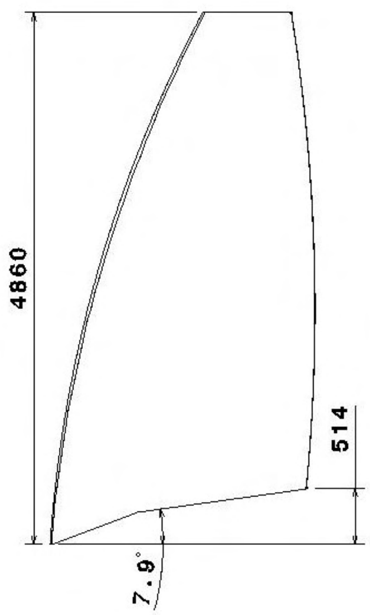

(a) Front view

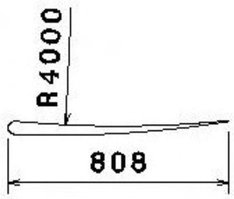

(b) Top view

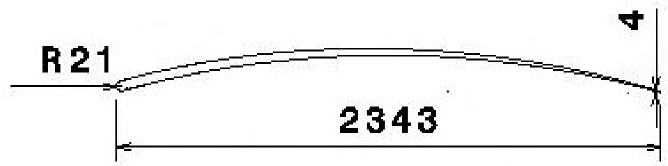

(c) Bottom view

Figure 3.3: Sail dimensions [mm]

3.3 Deck Sweepers

To investigate the effect of the aforementioned deck sweepers various versions have been modelled. The first being a typical triangular shaped decksweeper as shown in Figure 3.4a. The other most commonly used type is of a rectangular shape, two versions of this type were designed. The first having the same chord as the triangular version as shown in Figure 3.4b. The last version has an increased chord and thus extend further down the length of the sail. This also increases the aspect ratio from 2.56 for version 1 (V1) to 3.02 for the second version (rectangular V2).

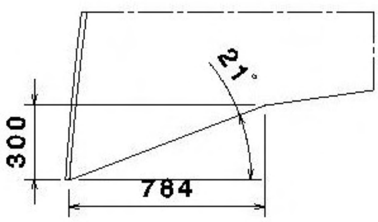

(a) Triangular, A ≈ 0.118 m^2

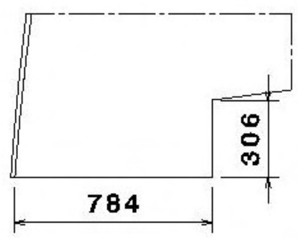

(b) Rectangular V1, A ≈ 0.234 m^2

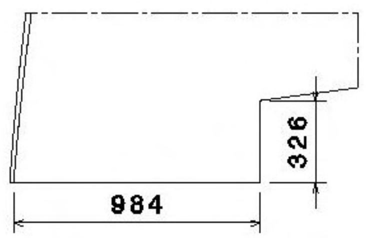

(c) Rectangular V2 (extended), A ≈ 0.321 m^2

Figure 3.4: Different deck sweeper panels dimensions [mm]

4
CFD Simulations

The chapter includes the approach to the CFD analysis performed on the previously designed CAD model. STAR-CCM+ is used for the meshing, analysis and post processing. Firstly, the coordinate system and decomposition of forces and velocities is described in Section 4.1. The defined computational domain is explained in Section 4.2. The meshing process and the mesh sensitivity study are discussed in Sections 4.3 and 4.4 respectively. The numerical settings are described in Section 4.5 and lastly the setup parameters are stated in Section 4.6.

4.1 Coordinate System & Decomposition of Forces and Velocities

The defined coordinate system is shown in Figure 4.1. The positive X-direction is along the right wing of the Moth, the Y-direction is positive along the length of Moth to the front of the hull and the Z-axis is positive towards the top of the sail.

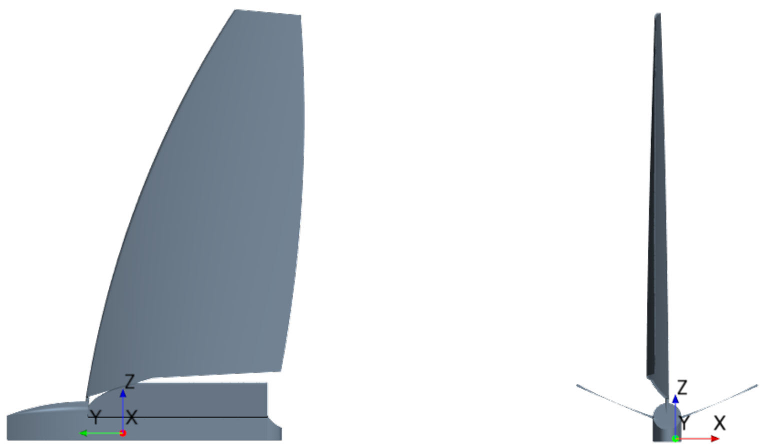

(a) Side view

(b) Rear view

Figure 4.1: Defined coordinate system

It is also important to establish the relevant velocities and the forces acting upon the Moth. The main points of sail is shown in Figure 4.2, where V_T is the true wind velocity, V_A is the apparent wind velocity and V_B is the boat velocity. The area indicated in red is the so called "no-go" zone where no propelling force is generated from the sail. The letters A to E indicate different points of sail, which have the following predominant sail force components:

- A. Luffing (no propulsive force) - 0-30°
- B. Close-Hauled (lift) - 30-50°
- C. Beam Reach (lift) - 90°
- D. Broad Reach (lift-drag) - ∼135°
- E. Running (drag) - 180°

The force components are defined as shown in Figure 4.3, where F_T is the total aerodynamic force. This force has a component is in the direction of the apparent wind D (drag) and L (lift) perpendicular to the drag component. The forces are also decomposed into F_R and F_{LAT}. F_R is in the direction of the velocity of the boat and is the driving force, F_{LAT} is the lateral force causing a heeling force. The non-dimensional coefficients of the lift and drag forces, C_{L_A} and C_{D_A} respectively, are calculated as in equations 4.1 and 4.2. Where L and D are the aforementioned forces, ρ is the air density, v the free stream velocity and A_{sail} the sail area. An important performance metric to assess the efficiency of the sail is the ratio C_{L_A}/C_{D_A}.

$$C_{L_A} = \frac{2 * L}{\rho * V_A^2 * A_{sail}} \quad (4.1)$$

$$C_{D_A} = \frac{2 * D}{\rho * V_A^2 * A_{sail}} \quad (4.2)$$

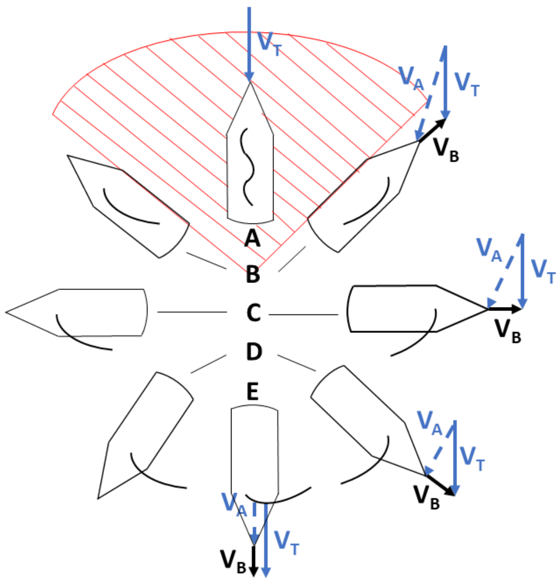

Figure 4.2: Points of sail [17]

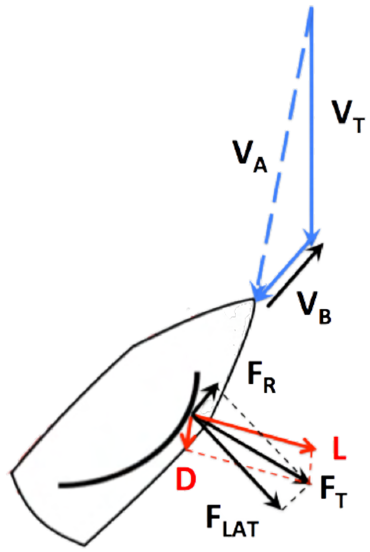

Figure 4.3: Defined force components [17]

4.2 Computational Domain

The domain was designed such that it accommodates a wide range of apparent wind angles, ranging between approximately 24 and 40 degrees. The width, length and height of the domain were chosen in such a way to minimize the effect of the boundary conditions on the results of the simulations, while keeping the computational costs of the mesh at a reasonable level. The dimensions of the domain are shown in Figure 4.4, the indicated inlet and outlet types will be explained further in Section 4.5.

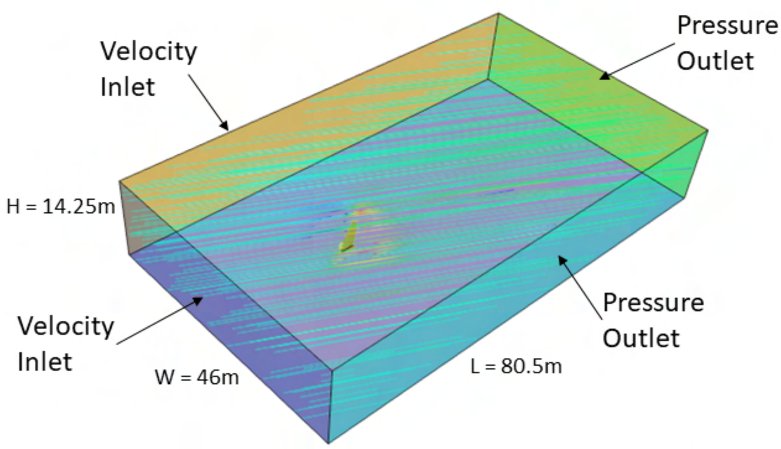

Figure 4.4: Computational domain

The boundary conditions of the domain must be set and the physicals model to be used in the simulations must be selected.

- **Inlets**: Velocity inlets, the magnitude is varied for each set apparent wind angle, which is discussed further in Section 4.6.
- **Outlets:** Pressure outlets.
- **Roof:** Symmetry plane.
- **Ground:** Symmetry plane.

The Moth is placed at 24 m from the head on velocity inlet in the negative Y-direction, and 4 m in the positive X-direction to allow the wake to be fully captured. To simulate the distance to the water when the model is foiling, the Moth is placed at 500 mm above the ground.

4.3 Mesh

With the domain defined and the boundary conditions set, the meshing of the domain needs to be done. For this the surface remesher, automatic surface repair, trimmed cell mesher and prism layer mesher were selected.

4.3.1 Surface Mesh

The surfaces of the domain and the Moth were defined with the surface remesher. The aim was to have a larger cell size near the boundaries of the domain and smaller cell sizes near the Moth and its surface to ensure good accuracy while limiting computational cost. Refinement regions were defined to ensure proper capture of the wake and up-wash. Furthermore, smaller cell sizes were needed around certain curves in the model of the Moth. Figure 4.5 shows the mesh around the Moth itself. Automatic surface repair is often used with wrapped surfaces and repairs any problems with pierced faces, surface proximity and surface quality.

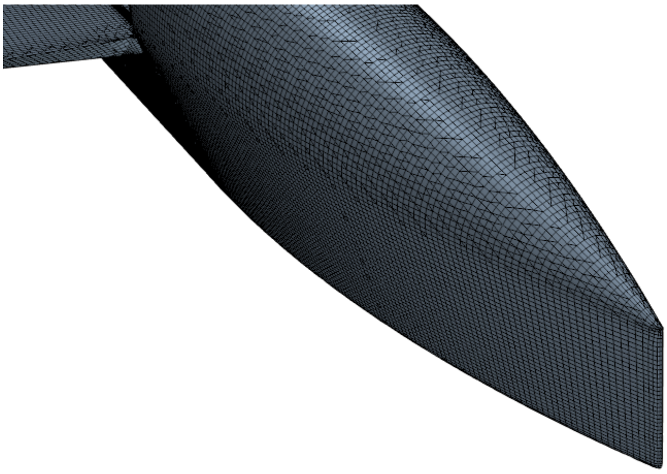

Figure 4.5: Surface mesh

4.3.2 Volume Mesh

The trimmed cell mesher is used for the volumetric mesh, it is a commonly used meshing model and produces more accurate solutions compared to a tetrahedral mesh. Furthermore, the trimmer model is not directly dependent on the starting surface and produces a good quality mesh for most situations [14]. A top and side view of the mesh in the entire domain is shown in Figure 4.6, it shows the larger cell size away from the model, as well as the refinement around the Moth and in its wake. The wake region itself is also divided into several areas with decreasing cell size near the Moth and the angle of the wake refinement corresponds to the set angle for the inlet velocity. The refinement boxes around the Moth, that capture complex flow such as the up-wash, can be seen in Figure 4.7.

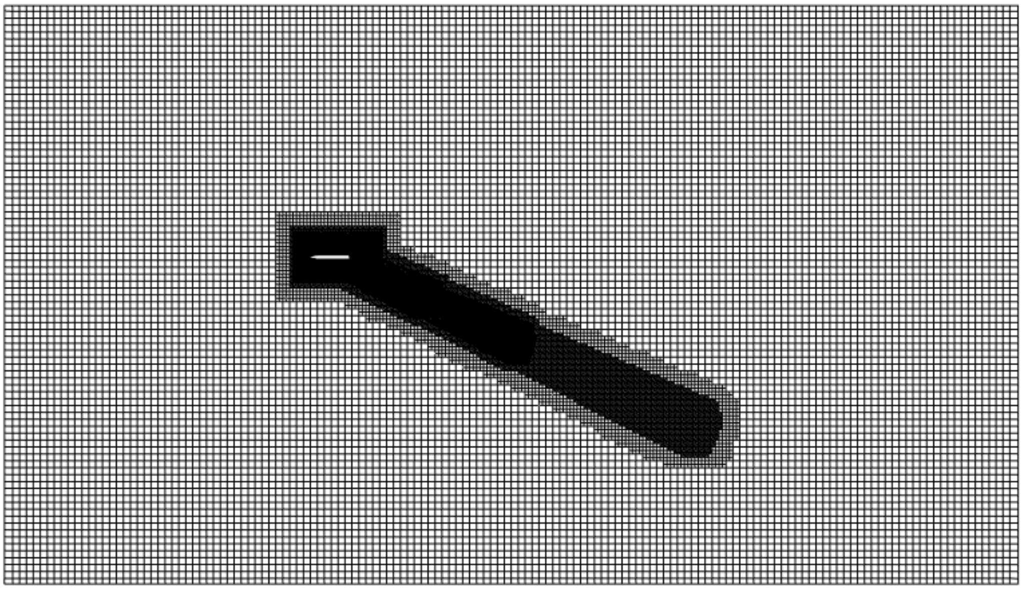

(a) Top view

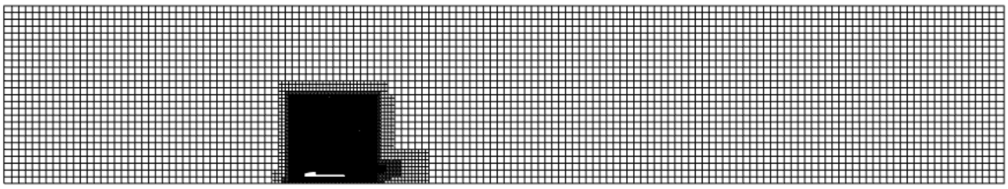

(b) Side view

Figure 4.6: Volume mesh of the complete domain

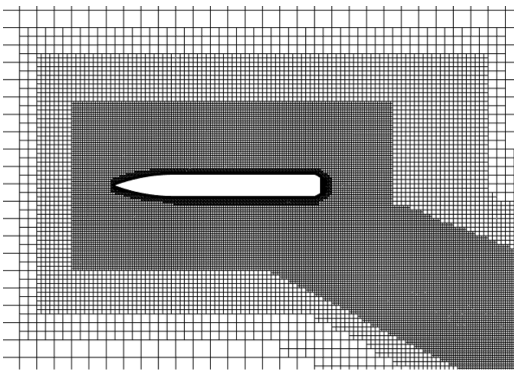

(a) Top view

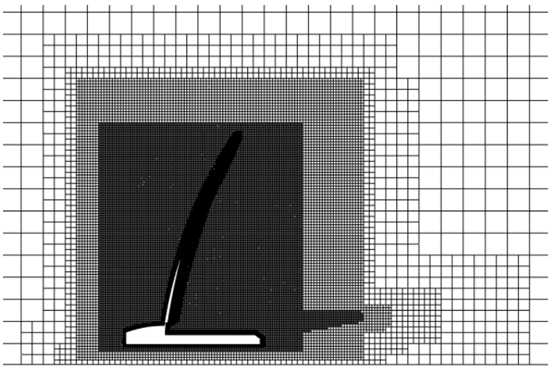

(b) Side view

Figure 4.7: Mesh refinement blocks

To capture the boundary layer formation the prism layer mesher is used. All y^+-treatment is used as this aims to model the boundary layer with a wide range of the first cell height for low $y^+ < 1$ and high $y^+ > 30$. Wall y^+ is defined as:

$$y^+ = \frac{y * u_T}{\mu} \tag{4.3}$$

With y^+ being the first cell thickness, u_T the friction velocity and μ the kinematic viscosity of the fluid. It was decided to use 12 prism layers and aim for a y^+ of around 50. The mesh around the sail is shown in Figure 4.8 and the prism layers in Figure 4.9.

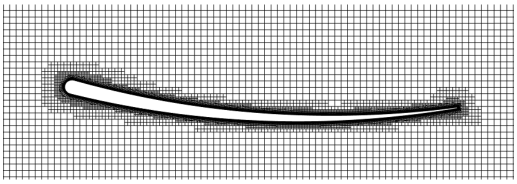

Figure 4.8: Mesh around the sail

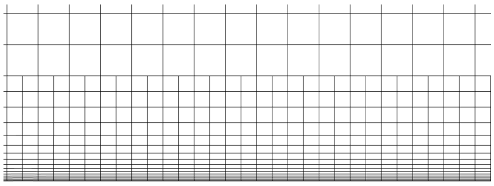

Figure 4.9: Prism cells near the wall

4.4 Mesh Sensitivity Study

A mesh sensitivity study was performed to select a mesh which provides reliable results while not being too computationally expensive. The sizing of cell was done relative to a baseline cell size, by changing this baseline cell size the mesh is refined or coarsened. Meshes ranging from approximately 5 to 20 million cells were generated. A simulation was run for each mesh and the forces and force coefficients were monitored. Determining if a simulation was converged was mainly done by analysing the forces acting upon the Moth as shown in Figure 4.10. The residuals were also used as a second indicator. When the oscillations in the forces were limited, the simulation was determined to be converged.

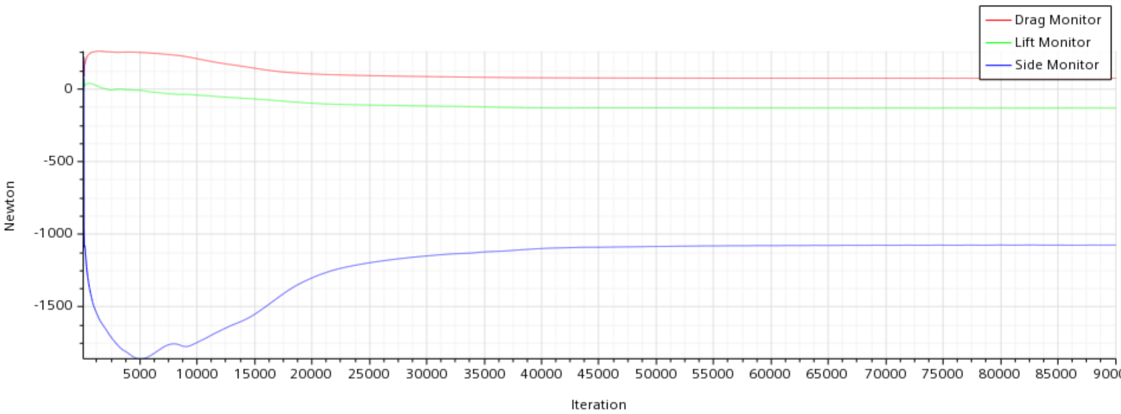

Figure 4.10: Typical monitor to determine convergence

The graphs in Figure 4.11 show that the changes in the drag coefficient are small, larger differences can be seen in the lift coefficient. However, between 12 and 20 million cells this change is significantly smaller and with the computational cost kept in mind, the 12 million mesh size was selected.

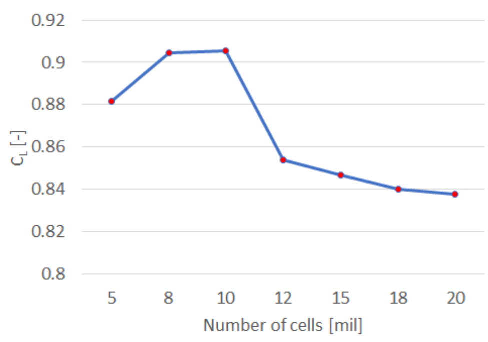

(a) Lift coefficient

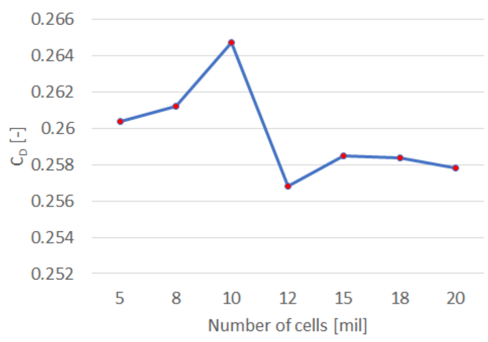

(b) Drag coefficient

Figure 4.11: Force coefficients versus mesh size

4.5 Physics & Solver Settings

The following physics and solver settings were selected for the simulations:

- **Three dimensional:** The scope of the thesis requires a three dimensional analysis.
- **Gas:** The fluid of interest is air.
- **RANS:** Reynolds Average Navier Stokes.
- **Constant density:** Incompressible flow is assumed as the fluid velocity does not exceed Mach 0.3. [1] Thus, constant density is selected.
- **Implicit unsteady flow:** Implicit unsteady flow was selected as the flow was predicted to have oscillations due to the large wind angles. This was confirmed by running a steady state simulation, which did not converge.
- **All y^+-wall treatment:** robust wall treatment which allows for a larger range of y^+-values.
- **Coupled flow solver:** this solver is selected as a complex flow is expected and this solver commonly has robust convergence.
- **k-epsilon turbulence model:** provides a good compromise between robustness, computational cost and accuracy [14].

4.6 Setup Parameters

Two of the main parameters to be set for each simulation are the apparent wind speed (AWS) and apparent wind angle (AWA) as described previously. To determine these parameters first the true wind angles (TWA) that are of interested need to be established. Taking into account the average duration of a simulation from the mesh sensitivity study it was decided to run a total of 18 simulations, six TWA's per deck sweeper type. The chosen angles are: 40, 45, 55, 75, 110 and 120 degrees. The angles were chosen based on what are common angles used in sailing. The true wind speed was chosen to be 9 m/s (17.5 kn) as this would result in an average cruising condition for the Moth.

The resulting boat velocity (V_B) is determined from the work performed by [10]. As mentioned previously his work included a polar plot showing the boat velocity versus true wind angles at different true wind speeds, shown in Figure 4.12.

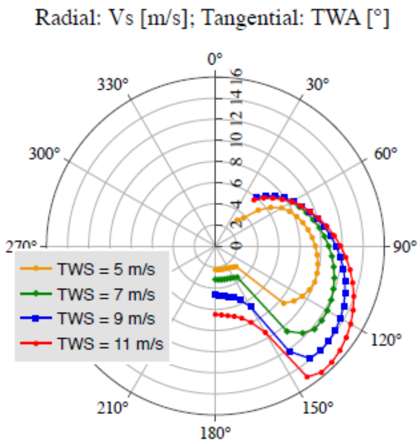

Figure 4.12: Polar plot of the Moth boat speed [10]

From the blue line in this figure the boat speeds were determined as stated in the Table 4.1. The AWS's and AWA's were then calculated using simple trigonometry equations 4.4 and 4.5.

$$V_A = \sqrt{V_T^2 + V_B^2 + 2V_T V_B \cos\alpha} \quad (4.4) \qquad \beta = \arccos\left(\frac{V_T \cos\alpha + V_B}{V_A}\right) \quad (4.5)$$

Table 4.1: Used AWA (β) and AWS (V_A) values based on TWA's (α), TWS's (V_T) and boat speeds (V_B) from [10]

TWA [°]	**TWS** [m/s]	**Boat Speed** [m/s]	**AWS** [m/s]	**AWA** [°]
40	9	6.1	14.2	24.0
45	9	7.0	14.8	25.5
55	9	8.0	15.1	29.3
75	9	9.9	15.0	35.4
110	9	13.2	13.2	39.9
120	9	13.7	12.1	40.3

The final apparent wind speeds stated in Table 4.1 are implemented at the two inlet boundaries according to Figure 4.13.

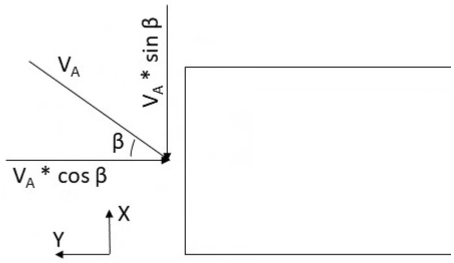

Figure 4.13: Relative velocity implementation

5 Results & Discussion

This chapter includes the results and discussions from the performed CFD simulations. Firstly, the general flow field is outlined and discussed in Section 5.1. Then, in Section 5.2 a more in depth look is taken at the influence of changing the true wind angle on the sail and different deck sweepers. Lastly, the overall forces and moments on the Moth are described in Section 5.3. Further flow visualisation can be found in Appendix B and complete tabulated data in Appendix C.

5.1 General Flow Field

The streamlines shown in Figure 5.1 give an idea of the flow behaviour around the Moth. The laminar flow upstream is disturbed by the hull, wings and sail of the Moth. The red shaded streamlines indicate the higher velocity flow on the leeward side of the sail. At the head of the sail the streamlines are directed upwards which is more clearly seen when looking at Figure 5.1b. The tip vortices due to the pressure difference between the windward and leeward side can be seen here. An increased flow velocity can be observed below the hull, the flow is then directed upwards along the lower part of the left wing as shown in Figure 5.1c.

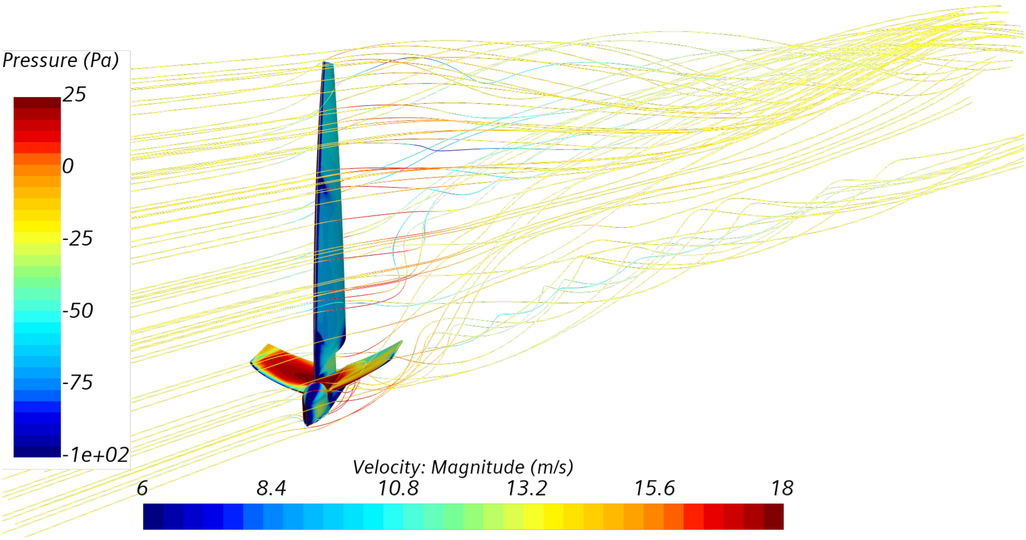

(a) Isometric view

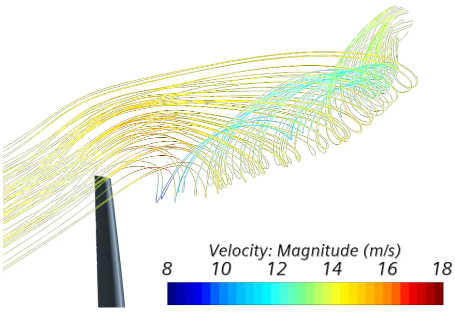

(b) Tip vortices at the head

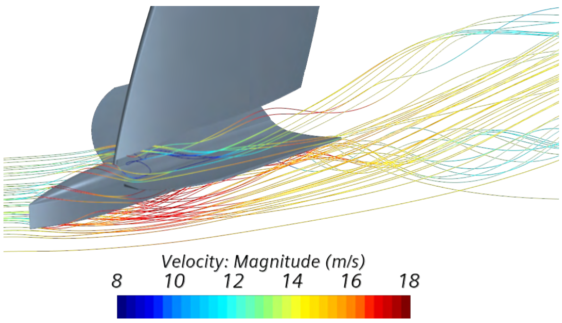

(c) Increased flow velocity below the hull

Figure 5.1: Typical streamlines around the Moth

A typical pressure field of the domain is show in Figure 5.2. There are a number of phenomena to point out here. There is a clear high pressure area directly in front of the Moth which decreases in intensity in the direction of the wind. While directly below the Moth a low pressure area is created. As mentioned previously, the velocity accelerates between the hull and the bottom boundary of the domain which corresponds to the waterline in a real life scenario, creating a Venturi effect. This increase of the flow velocity can also been seen in Figure 5.3d, where the red shade indicates a higher flow velocity. Furthermore, a thin low pressure wake which extends far away from the Moth is also clearly visible.

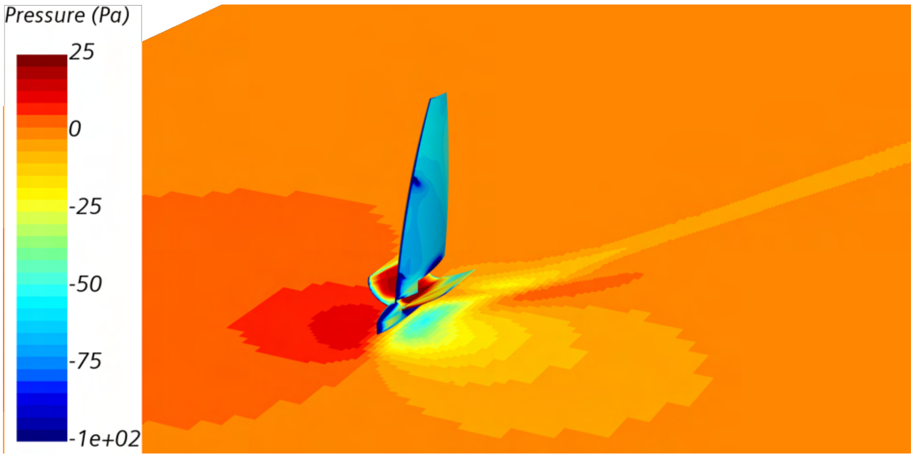

Figure 5.2: Typical pressure field (TWA: 40, deck sweeper: triangular)

Velocity contours of the flow field are shown in Figure 5.3 (the indicated z-locations of the planes are henceforth with respect to the bottom of the hull). The hull cross section shows that due to sharp design the flow separates at the bow, while at the rounded off stern the flow remains attached longer. The side view shows the higher flow velocity over the front part of the deck, and a recirculation region directly behind where the deck drops down to the part where the wings are attached. A similar but smaller region can be seen at the stern, where the hull has an indent (see Figure 3.2a), this is where normally the rudder assembly is attached. When comparing Figures 5.3b and 5.3c one can see the differences in the flow along the height of the sail. Lower down, at the deck sweeper the flow remains attached to the sail, where as at the middle section the sail the flow separates early on along the chord.

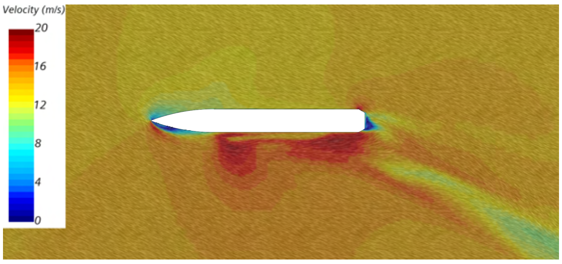

(a) z = 0.2 m

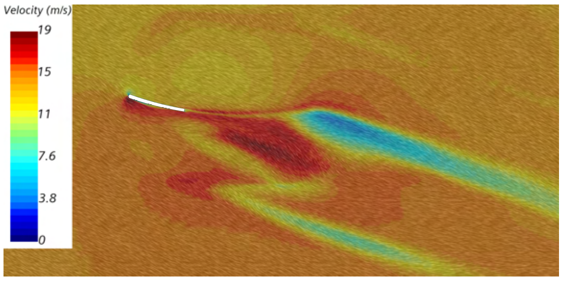

(b) z = 0.75 m

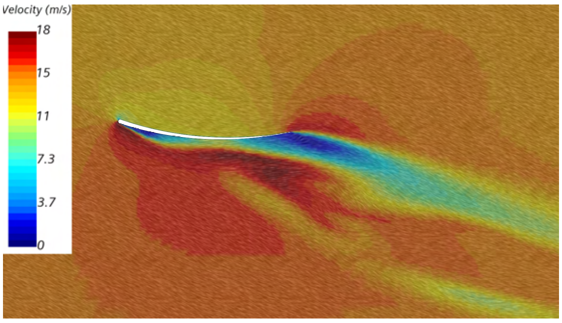

(c) z = 3 m

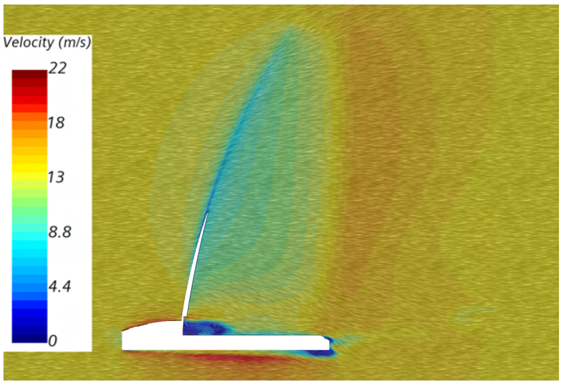

(d) Side view

Figure 5.3: Vector velocity fields of the flow field

5.2 Performance of the Sail & Deck Sweepers

5.2.1 Polar Plots: Dimensionless Coefficients

Several polar plots have been produced showing how the performance of the sail is influenced by the TWA. The lift and drag coefficients with respect to the apparent wind angles and their ratio are shown in Figure 5.4. C_{L_A} varies between 0.8 at 40° and 0.85 at 120°, the differences between the different deck sweepers are relatively small, however at a TWA of 55° a clear increase for the triangular deck sweeper can be seen compared to the other two. The drag coefficient shows a larger range of values from 0.27 at 40° to 0.58 at 120°, this is as expected. As the apparent wind angle increases the drag component of the total sail force increases. This also results in the ratio between the two coefficients to decrease from around 2.9 at 40° to around 1.45 at 120°.

Comparing with the previously mentioned work by Bögle [6], the change in lift coefficient is smaller, while the drag coefficient does show a similar trend of increasing with increasing wind angle. It should be noted that Bögle predicted the coefficients with respect to the EWA$_{eff}$ which also takes into account the heeling angle.

Table 5.1 includes the values for C_{L_A}/C_{D_A} and the change of the rectangular deck sweepers compared the the triangular version is shown. In general a small improvement is made when changing to the a rectangular deck sweeper, except at a TWA of 45°. The larger aspect ratio of the rectangular V2 deck sweeper shows a very limited improvement over the lower aspect ratio version.

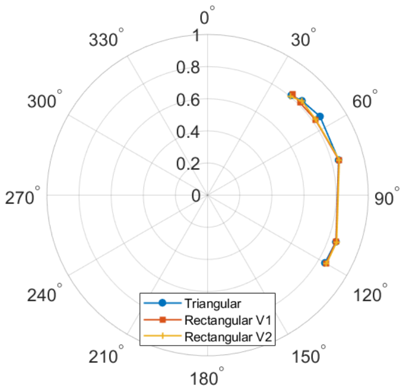

(a) Radial: C_{L_A} [-]; Tangential: TWA [°]

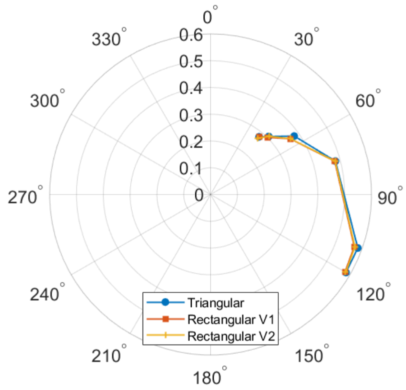

(b) Radial: C_{D_A} [-]; Tangential: TWA [°]

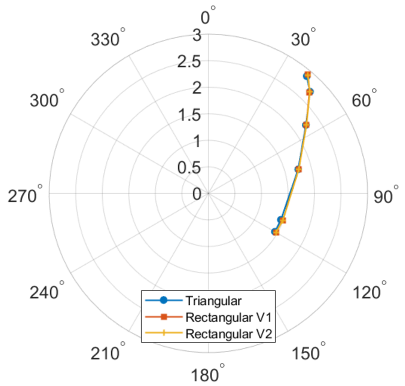

(c) Radial: C_{L_A}/C_{D_A} [-]; Tangential: TWA [°]

Figure 5.4: Polar plots C_{L_A}, C_{D_A} and C_{L_A}/C_{D_A} (sail)

Table 5.1: Ratios of the lift and drag coefficients (sail)

TWA [°]	C_{L_A}/C_{D_A} [-]			C_{L_A}/C_{D_A} **Compared**		
	Trian.	Rect. V1	Rect. V2	Trian.	Rect. V1	Rect. V2
40	2.8823	2.9222	2.9145	-	1.383%	1.114%
45	2.7084	2.6923	2.7016	-	-0.596%	-0.251%
55	2.2430	2.2550	2.2580	-	0.537%	0.669%
75	1.7514	1.7635	1.7648	-	0.688%	0.763%
110	1.4543	1.4906	1.4919	-	2.498%	2.584%
120	1.4466	1.4685	1.4694	-	1.509%	1.572%

5.2.2 Polar Plots: Force Components

The different force components, as explained in Section 4.1, are shown in Figure 5.5. The lift force L increases slightly up to a TWA of 75° after which it decreases faster to around 600N. While the drag force increases rapidly from approximately 270N at 40° to 520N at 75°, it then decreases slightly again up to 120°. A clear improvement in the driving force, the force component in the direction of the boat velocity, can be seen at TWA's 40°, 75°, 100° and 120°. The rectangular deck sweepers show an increase of the force of around 5% compared to the triangular version at these wind angles. Lastly, the lateral force component starts at a value of around 830N, then increases until its maximum is reached at ≈1050N and lowers again to around 730N. Complete tabulated data can be found in Appendix C.

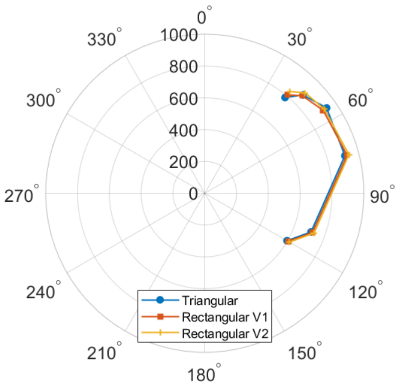

(a) Radial: L [N]; Tangential: TWA [°]

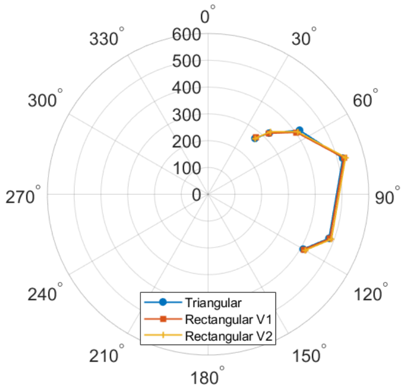

(b) Radial: D [N]; Tangential: TWA [°]

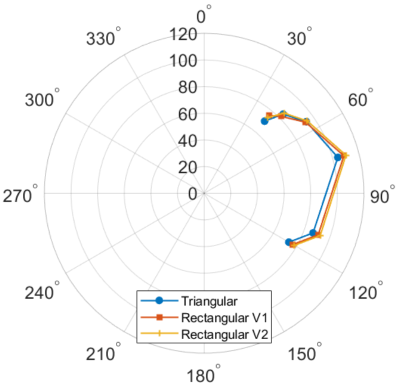

(c) Radial: F_R [-]; Tangential: TWA [°]

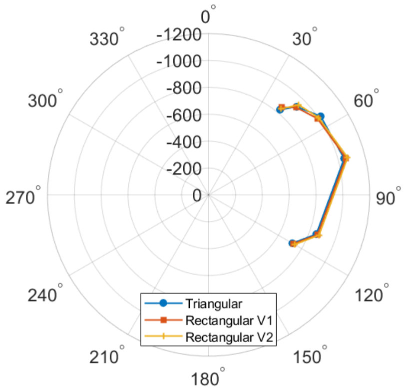

(d) Radial: F_{LAT} [-]; Tangential: TWA [°]

Figure 5.5: Polar plots L, D, F_R and F_{LAT} (sail)

5.2.3 Pressure Distribution

The pressure coefficient C_p is a dimensionless coefficient and is defined as follows [8]:

$$C_p = \frac{p_{stat} - p_{\infty,stat}}{p_{\infty,dyn}} = \frac{p_{stat} - p_{\infty,stat}}{\frac{1}{2}\rho_\infty v_\infty^2} \tag{5.1}$$

Where p_{stat} is the static pressure in the point of evaluation, $p_{\infty,stat}$ the static pressure in the free stream flow and $p_{\infty,dyn}$ the dynamic pressure in the free stream flow.

The distribution of the pressure coefficient along the chord of the sail is shown in Figure 5.6. The windward side of the sail shows a typical pressure distribution, a high pressure area occurs at the luft where the flow stagnates, it then decreases slowly and as it reaches the trailing edge of the sail the pressure drops rapidly. This distribution is also clearly visible in Figure 5.7. Here the difference between the drop-off of the pressure coefficient between the different deck sweepers can also be seen. The increased sail area of the rectangular deck sweepers up to around 0.4c slows the drop-off of the pressure.

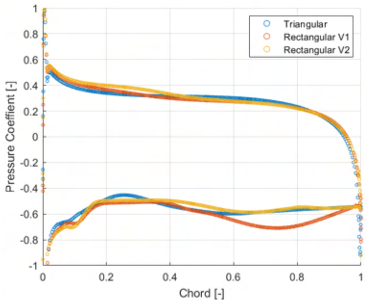

(a) TWA: 40°

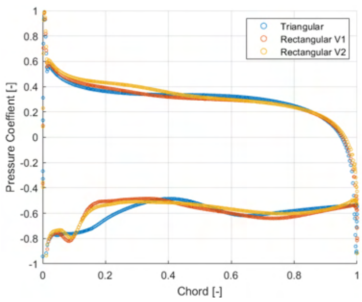

(b) TWA: 45°

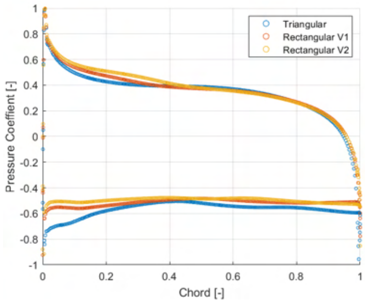

(c) TWA: 55°

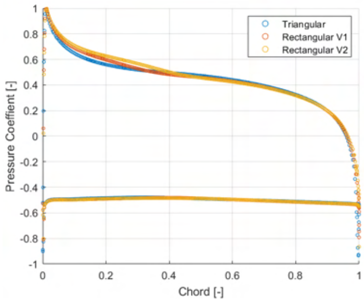

(d) TWA: 75°

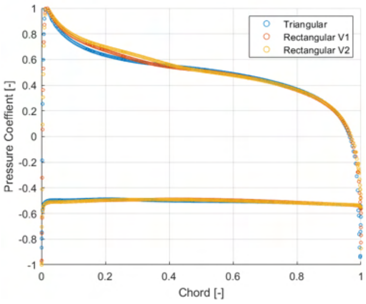

(e) TWA: 110°

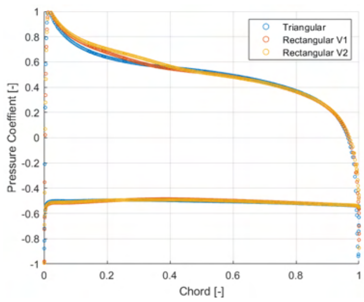

(f) TWA: 120°

Figure 5.6: Pressure coefficients along sail chord at z = 1 m

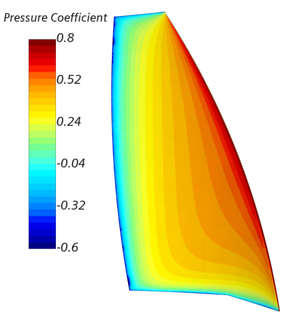

(a) TWA: 40°, Triangular

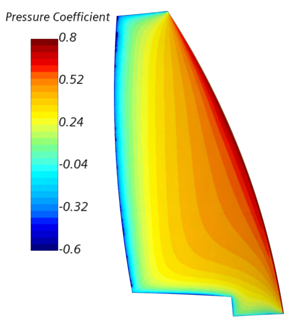

(b) TWA: 40°, Rectangular V1

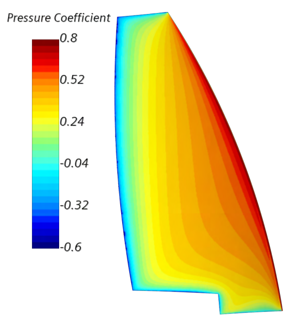

(c) TWA: 40°, Rectangular V2

Figure 5.7: Pressure coefficient windward side (sail view)

Looking at the leeward side in the pressure distribution it is clear that at lower TWA's there is is some variation between the different deck sweepers, while from 75° onward the distribution stabilises. This can also be seen when looking at the distribution of the pressure coefficient shown in Figure 5.8. The first figure shows the higher pressure area on the deck sweeper and the lower pressure area from $\approx 0.4c$. This lower pressure region disappears as the wind angle increases. From all figures there is also a clear higher pressure at the leech which becomes more concentrated as the TWA increases. The maximum of these pressure zones seems to correspond to where the leech curvature is at its maximum. Lastly, the rectangular V1 decksweeper at a 40° TWA case shows a very low pressure area at the luff around half way up the sail. This is the only case where this phenomena occurs out of all simulations. Figure 5.9 shows the streamlines along the sail for this case. This area also shows an increase in the wall shear stress pressure as explained in Section 5.2.4. It is not clear what causes this lower pressure area only in this specific case.

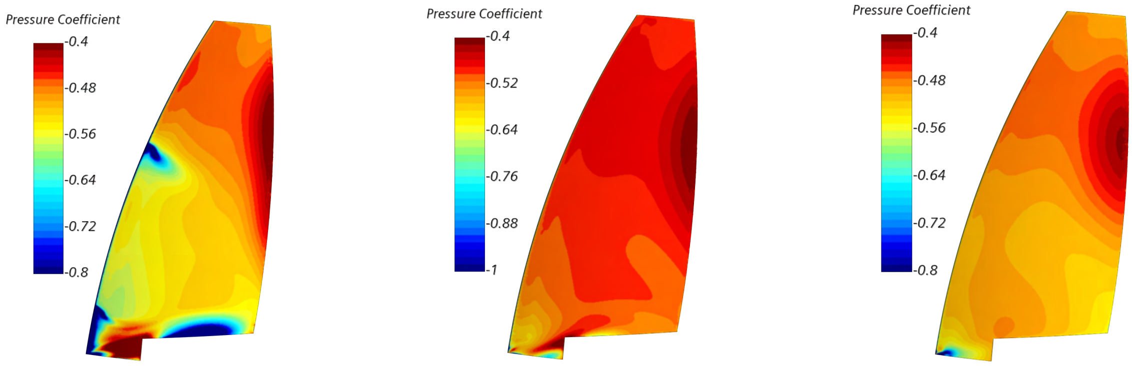

(a) TWA: 40° **(b)** TWA: 55° **(c)** TWA: 120°

Figure 5.8: Pressure coefficient leeward side (sail view, rectangular V1)

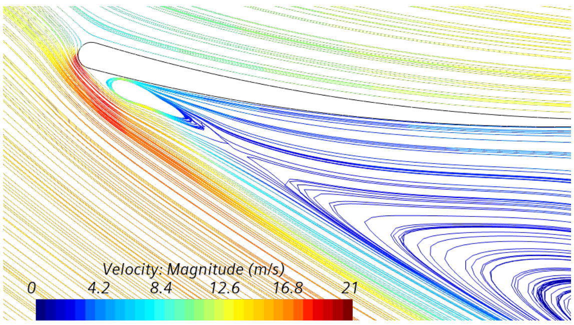

Figure 5.9: Streamlines luff (TWA: 40°, Rectangular V1)

The previously made comparison of C_{L_A}/C_{D_A} ratios between the different deck sweepers showed overall a small increase in performance for the rectangular versions compared to the triangular version. Except at a TWA of 45° a small decrease was observed, an explanation for this can be observed in Figure 5.10. The sail with the triangular deck sweeper in this case shows a larger region with a lower pressure coefficient at the luff compared to the other versions. This could be an explanation in the relative performance difference.

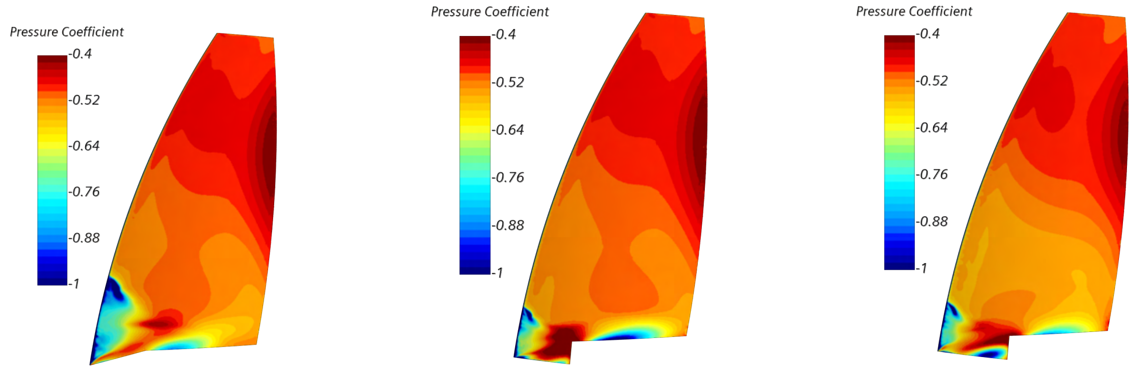

(a) Triangular **(b)** Rectangular V1 **(c)** Rectangular V2

Figure 5.10: Pressure coefficient leeward side (sail view, TWA: 45°)

5.2.4 Flow Separation

An interesting phenomena to look at is separation of the flow, if it occurs and when it occurs. The wall shear stress τ_w can give a good indication of flow separation and it is defined as [9]:

$$\tau_w = \mu \left(\frac{\delta u}{\delta y} \right)_{y=0} \tag{5.2}$$

Where μ is the dynamic viscosity, u is the flow velocity parallel to the wall and y is the distance to the wall. Resulting plots along the bottom section of the sail are shown in Figure 5.11. Again there is a clear distinction between the lower and higher TWA's on the leeward side of the sail. At the lower TWA's the flow is in some cases still attached while from 75° onward the flow is fully separated and the wall shear stress is minimal. When taking a closer look at the results for a TWA of 55° there is are some differences between the different deck sweepers. Streamlines of the cases are shown in Figure 5.12, these explain the wall shear stress distribution. The flow is fully separated for the rectangular V2 case which can be seen as the low τ_w in the plot. In both the triangular and the rectangular V1 case, the flow first separates, resulting in a dip in τ_w, and then reattaches again, increasing τ_w again. However, the turbulent reattachment point occurs earlier along the chord for the triangular case, in this the case the turbulent flow detaches again near the trailing edge, similar to the flow regions described in Figure 2.2.

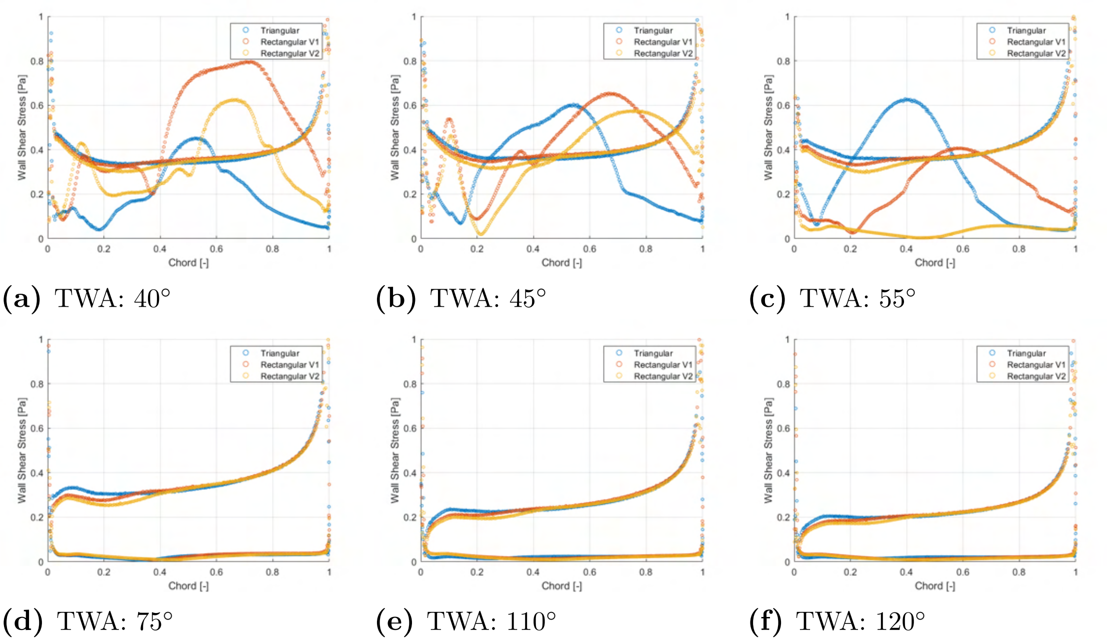

(a) TWA: 40° **(b)** TWA: 45° **(c)** TWA: 55°

(d) TWA: 75° **(e)** TWA: 110° **(f)** TWA: 120°

Figure 5.11: Wall shear stress along sail chord at z = 1 m

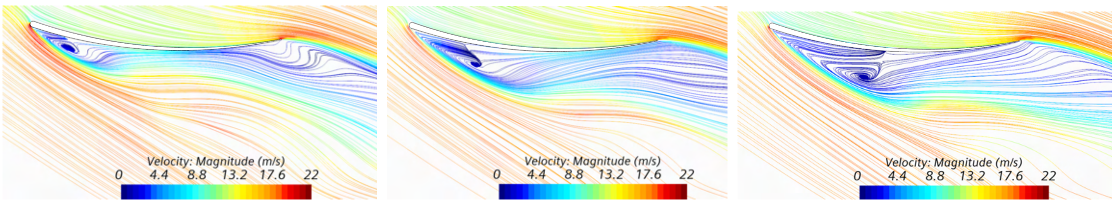

(a) Triangular **(b)** Rectangular V1 **(c)** Rectangular V2

Figure 5.12: Streamlines at z = 1 m (TWA: 55°)

It is also interesting to look at how the flow changes from the foot to the head of the sail. The flow variation along the height of the sail for a typical case is shown in Figure 5.13. At the lower sections the flow mostly remains attached to surface while further towards the head flow separation occurs early on. The middle and top section show significant recirculation regions, a similar result was observed for all cases.

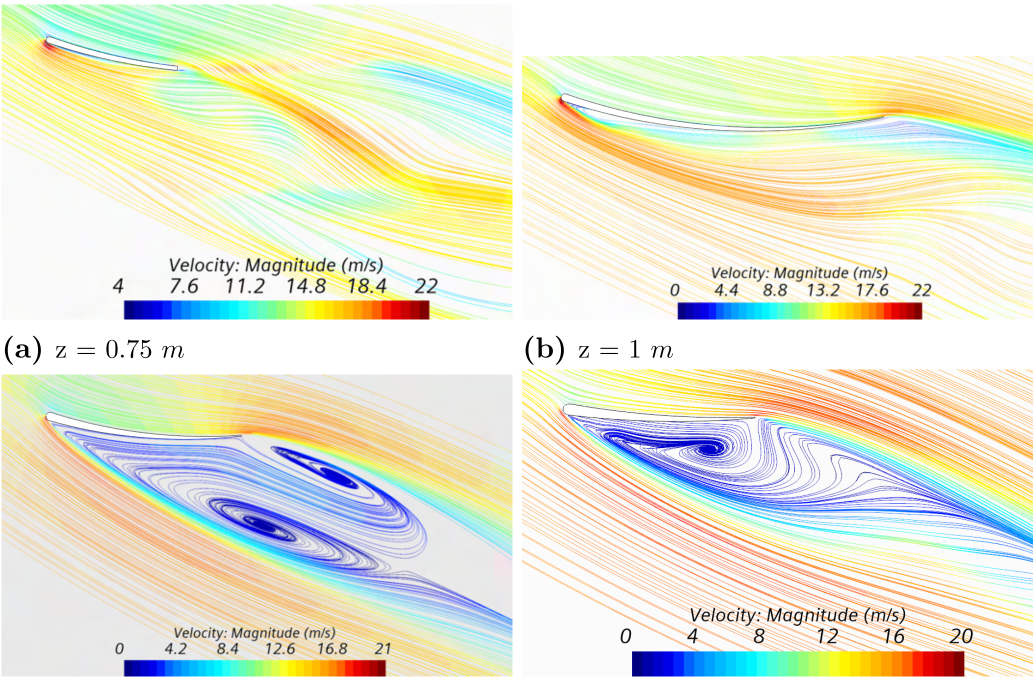

(a) z = 0.75 m **(b)** z = 1 m

(c) z = 3 m **(d)** z = 5 m

Figure 5.13: Variation in flow along the height of the sail (TWA: 40°)

5.3 Forces & Moments on the Moth

5.3.1 Forces on the Hull & Wings

The forces on the hull and wings are tabulated in Table 5.2. F_R acts in the direction of the boat velocity (y-direction) and can thus be considered as drag, the values are relatively small due to the streamlined design of the Moth. As expected the drag force decreases as the wind angle increases. Complete tabulated data can be found in Appendix C.

Regarding the lateral forces, these are more significant for both the hull and the wings. These forces can easily be explained when looking at the differences between the pressure coefficient on the windward and leeward side, as shown in Figure 5.14. On the windward side the pressure is high at the bow and then decreases along the length of the hull towards the stern. The hull and wings create a low pressure zone on the leeward side. It should also be noted that the hull and wings have a significant contribution, 14 to 20%, to the total lateral force. Where the hull contributes almost twice as much as the wings.

Table 5.2: Forces acting upon the hull and wings (triangular)

TWA [°]	F_R [N]		F_{LAT} [N]		F_Z [N]	
	Hull	Wings	Hull	Wings	Hull	Wings
40	-5.9	-4.6	-84.9	-49.0	-100.2	-37.6
45	-5.9	-4.8	-100.9	-57.6	-103.5	-47.4
55	-4.7	-4.7	-129.0	-77.0	-161.3	-84.6
75	-4.0	-3.1	-166.2	-102.8	-209.2	-141.3
110	-1.4	-2.3	-141.9	-87.5	-176.1	-110.6
120	-1.9	-2.0	-119.1	-73.7	-144.1	-88.7

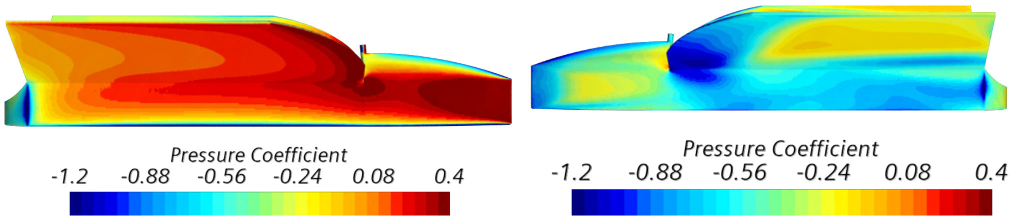

(a) Windward **(b)** Leeward

Figure 5.14: Pressure coefficient on the hull and wings (side view, TWA: 40°)

The different pressure zones on top and bottom side of the hull and wings are shown in 5.15. The negative vertical forces F_Z on the hull can be explained by the differences between the pressure zones on the top and bottom of the hull. Although the wings have a larger surface area, the negative vertical forces are lower than for the hull. This can be explained by the pressure coefficient on the bottom of the windward side wing (left wing in Figure 5.15b) being positive and thus offsetting the downforce generated by the leeward wing. The hull and wing combined result in downforce values of 130 to 350 N or approximately 13 to 35 kg. These are significant values as a typical Moths weight is below 30 kg. These negative vertical forces are of importance as they will need to be offset by the foils.

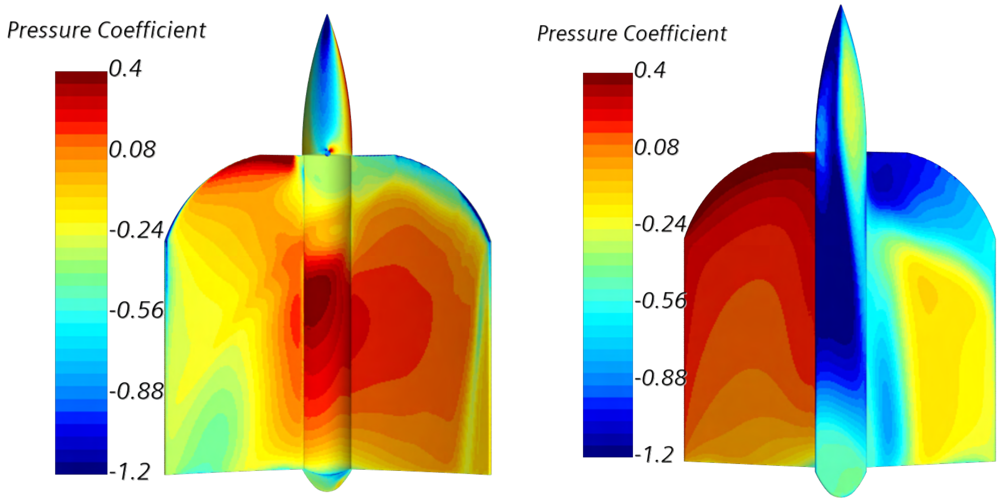

(a) Top view **(b)** Bottom view

Figure 5.15: Pressure coefficient on the hull and wings (TWA: 40°)

5.3.2 Moments on the Moth

The total moments around the different axis are stated in Table 5.3 (all data can be found in Appendix C). The origin of the axis was in this case taken to be where the mast connects to the hull. The moment around y-axis (M_y) is mainly attributed to the lateral force from the sail F_{LAT} and causes the Moth to roll (heeling). The relatively small M_x values cause the Moth to pitch which will need to be compensated by adjusting the front and aft foils. Lastly, M_z causes the Moth to yaw and is mainly influenced by the lateral force of the sail. To keep the heading of the boat, the rudder will need to compensate for this moment.

Table 5.3: Moments on the Moth (triangular)

TWA [°]	$\boldsymbol{M_x}$ **[Nm]**	$\boldsymbol{M_y}$ **[Nm]**	$\boldsymbol{M_z}$ **[Nm]**
40	-41.1	-1793.2	-1302.2
45	-34.5	-1993.2	-1455.1
55	11.9	-2217.7	-1646.8
75	84.3	-2295.4	-1754.0
110	49.8	-1872.7	-1439.6
120	30.7	-1582.0	-1213.3

6

Conclusions & Future Work

The work performed during the course of this thesis included the design of simplified parametric model of the International Moth class which was sequentially used for a CFD investigation into the aerodynamics of the class. The model was tested for a range of TWA's and the effect of different types of "deck sweepers" was assessed.

The Moth was simplified in a number of ways, such as removing the foils, gantry and rigging, as this would add unnecessary complexity. The CAD model was designed in a parametric way allowing easy modification of certain design parameters, such as the angle of the wings and sail, sail camber and chord. A setup for a CFD analysis was made, which included setting the correct flow conditions and meshing of the domain. The model with three different deck sweepers was tested for six true wind angles, resulting in a total of 18 simulations.

The pressure fields showed a high pressure up-wash in front of the sail and a low pressure area below the Moth where the flow is accelerated between the bottom of the hull and the lower boundary. A recirculation region is observed between the wings behind the higher part of the deck. Typical tip vortices at the head of the sail are visible, increasing induced drag.

The analysis of different TWA's showed a small decrease for the lift coefficient from ≈0.85 at 40° to ≈0.8 at 120° and a larger increase for the drag coefficient from ≈0.27 to ≈0.58. The rectangular deck sweepers resulted in an increase between 0.5% and 2.5% for the C_{L_A}/C_{D_A} ratio compared to the triangular deck sweeper except for a TWA of 45°, which showed a small decrease. The rectangular deck sweeper with a larger aspect ratio showed a very minimal performance increase compared to the lower aspect ratio deck sweeper. Flow separation along the complete height of the sail occurred from a TWA of 75° onward, while at lower TWA's some flow separation and reattachment still occurred at the lower parts of the sail.

The found drag forces of the hull and wings were small due to the tested wind directions, with the lateral forces being more significant. The hull and wings combined accounted for between 14 and 20% of the total lateral force. The hull and wings also resulted in downforce values of between 130 and $350N$ (≈13-35 kg), which is significant, when taking into account a typical rigged weight of the Moth of below 30 kg.

The CAD model could be further developed to be a more accurate representation of the Moth, where the aerodynamic effects of for example the foils and rudder can be included in the analysis. Furthermore, the parametric design of the sail could be further expanded, such as in the work performed by Cella et Al. (2017) [7]. This work included the parametric design of the sail through a Python script, allowing an optimization algorithm to be run together with RANS simulations. Another option would be the use of an aircraft airfoil, such as the modified NACA 4-digit airfoil. This would allow more customisation of both the mast and sail.

As the simulations were computationally intensive and resources were limited, a limited number of simulations could be performed. It would be interesting to perform more simulations while adjusting different parameters. Heeling of the Moth will most likely have a significant influence on its performance, as well as sail angle and camber. Further investigation of different deck sweepers and adjusting the gap between deck and sail could give more insight into gaining more performance.

The work performed assumed a rigid sail, which is not the case in the real world. The pressure from the wind deforms the sail, which changes the flow characteristics over the sail, as shown by Bak et al. (2013) [3]. It would be interesting to see the difference between a rigid and deformed sail for the Moth, however this is a complex analysis and would require a significant amount of time and resources.

Lastly, as there is very limited experimental data available for the Moth, it would be very interesting to perform wind tunnel tests. The CAD model as is, could be relatively easily modified to be 3D-printed, which in turn could be used in wind tunnel experiments. The resulting data could be used as validation of the found results in this thesis.

Bibliography

[1] John D Anderson. *Fundamentals of aerodynamics*. 6th ed. Columbus, OH: McGraw-Hill Education, 2016.

[2] Keith Bailey, Peter Jackson, and Richard Flay. “Modelling viscous flow around 2-D yacht mast and sail configurations”. en. In: *13th Australasian Fluid Mechanics Conference*. Auckland, New Zealand: University of Auckland, 1998.

[3] Sera Bak, Jaehoon Yoo, and Chang Yong Song. “Fluid-structure interaction analysis of deformation of sail of 30-foot yacht”. In: *Int. j. nav. archit. ocean eng.* 5.2 (2013), pp. 263–276.

[4] Bill Beaver and John Zseleczky. “Full Scale Measurements on a Hydrofoil International Moth”. en. In: *The 19th Chesapeake Sailing Yacht Symposium*. ANNAPOLIS, MARYLAND, Mar. 2009.

[5] Domenico Boffi. *Confirmed: 36.6 knots according Velocitek Prostart*. `https://web.archive.org/web/20181001195617/http://www.foilingweek.com/blog/2014/05/confirmed-36-6-knots-according-velocitek-prostart/`. Accessed: 2021-10-18. May 2014.

[6] Christian Bögle. “Evaluation of the Performance of a Hydro-Foiled Moth by Stability and Force Balance Criteria”. en. MA thesis. Berlin, Germany: TU-Berlin, Oct. 2010.

[7] Ubaldo Cella, Filippo Cucinotta, and Felice Sfravara. “Sail plan parametric CAD model for an A-class catamaran numerical optimization procedure using open source tools”. In: *Lecture Notes in Mechanical Engineering*. Cham: Springer International Publishing, 2017, pp. 547–554.

[8] L J Clancy. *Aerodynamics*. en. London, England: FT Prentice Hall, 1978.

[9] Corrosionpedia. *Wall Shear Stress*. `https://www.corrosionpedia.com/definition/1157/wall-shear-stress`. Accessed: 2021-11-3. Sept. 2013.

[10] Fabio Eggert. “Flight Dynamics and Stability of a Hydrofoiling International Moth with a Dynamic Velocity Prediction Program (DVPP)”. en. MA thesis. Berlin, Germany: TU Berlin, Aug. 2018.

[11] Heikki Hansen. “Enhanced Wind Tunnel Techniques and Aerodynamic Force Models for Yacht Sails”. en. PhD thesis. Auckland, New Zealand: The University of Auckland, 2006.

[12] Jonathan Ross. *MACH2.6 3D Rendering*. `https://www.mach2boats.com/index.php/the-mach-2-5/mach2-5-3d`. Accessed: 2021-10-19.

[13] *Rules and Documents*. `http://www.moth-sailing.org/history/rules-and-documents/`. Accessed: 2021-10-18.

[14] Siemens. *Simcenter STAR-CCM+ User Guide*. en. 2020.

[15] Ignazio Maria Viola. "Downwind sail aerodynamics: A CFD investigation with high grid resolution". en. In: *Ocean Eng.* 36.12-13 (2009), pp. 974–984.
[16] Wikipedia contributors. *Moth (dinghy)*. `https://en.wikipedia.org/w/index.php?title=Moth_(dinghy)&oldid=1038592630`. Accessed: 2021-10-18. Aug. 2021.
[17] Wikipedia contributors. *Point of sail*. `https://en.wikipedia.org/w/index.php?title=Point_of_sail&oldid=1019117711`. Accessed: 2021-10-24. Apr. 2021.
[18] Chris Williams. *Tuning Guide*. `http://usfoilingmoths.blogspot.com/2010/03/tuning-guide.html`. Accessed: 2021-10-27.

A
Technical Drawings

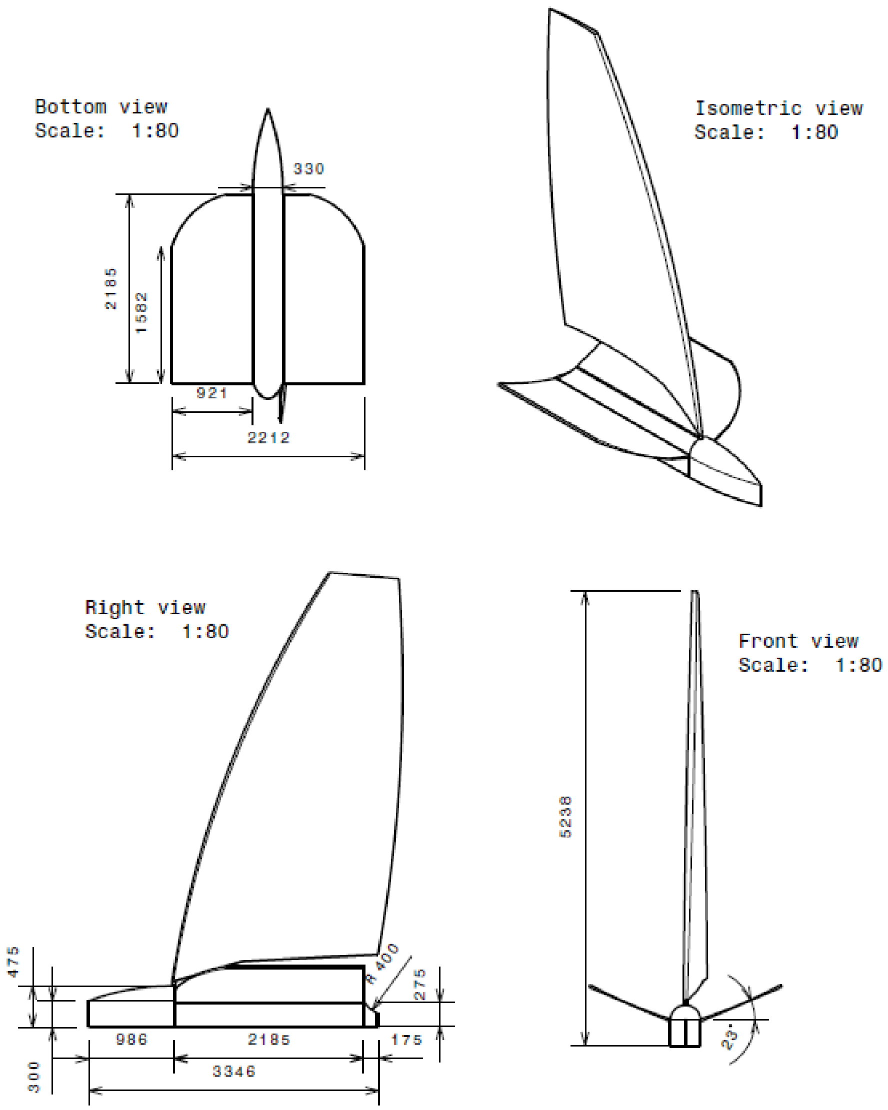

Figure A.1: Technical drawing of the Moth model (dimensions in *mm*)

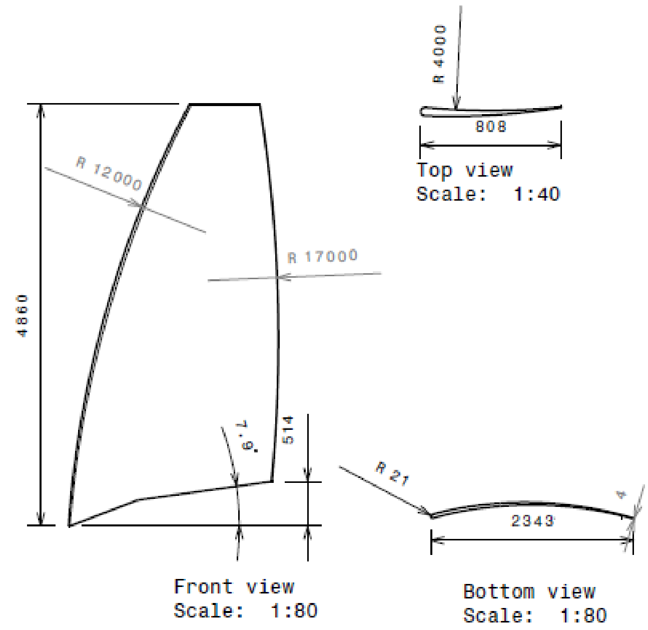

Figure A.2: Technical drawing of the sail (triangular) (dimensions in *mm*)

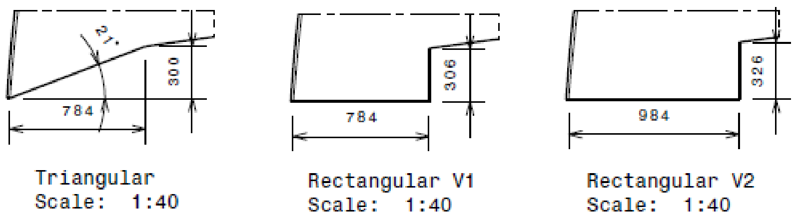

Figure A.3: Technical drawings of the deck sweepers (dimensions in *mm*)

B

Flow Visualisation

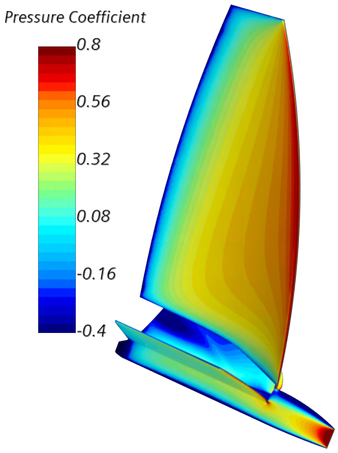

(a) TWA: 40°

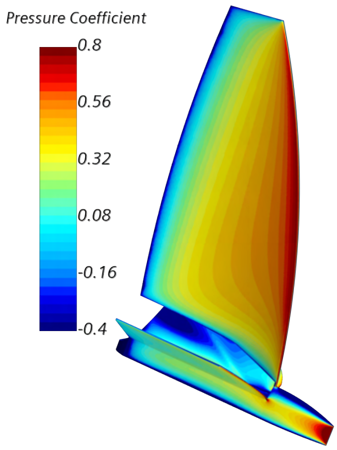

(b) TWA: 45°

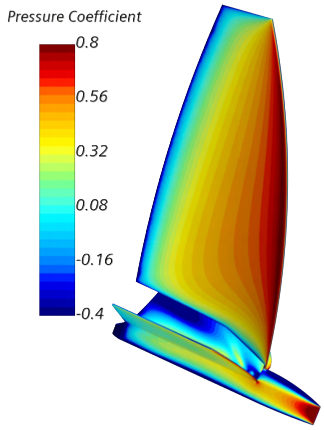

(c) TWA: 55°

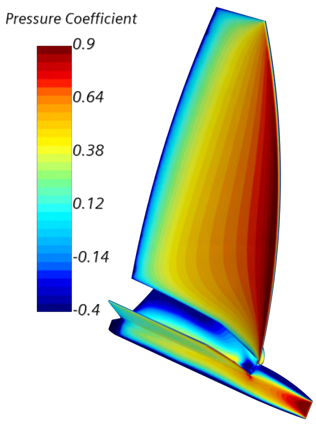

(d) TWA: 75°

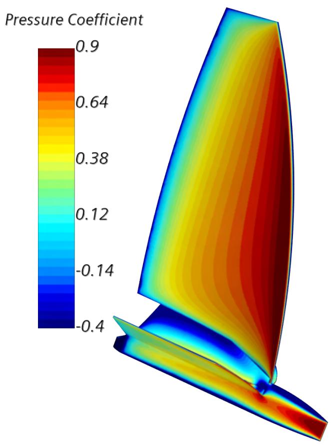

(e) TWA: 110°

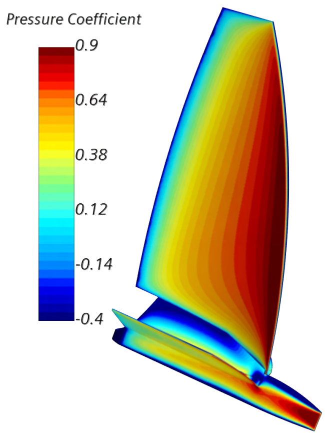

(f) TWA: 120°

Figure B.1: Pressure coefficient windward side (ISO view, triangular)

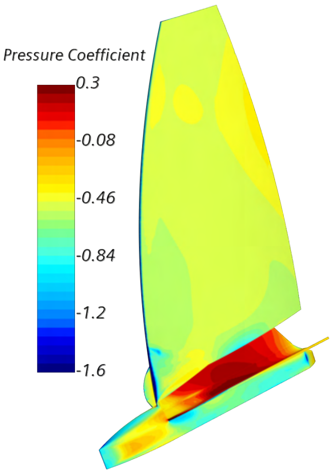

(a) TWA: 40°

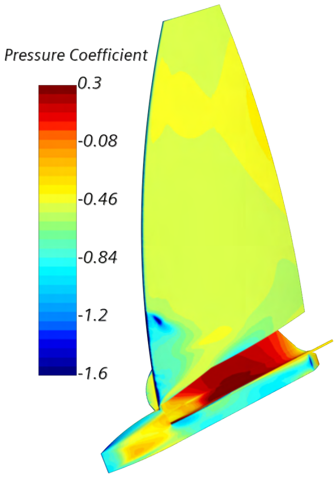

(b) TWA: 45°

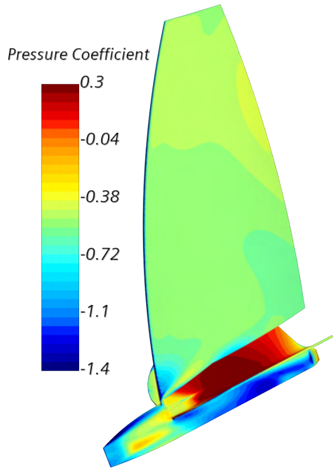

(c) TWA: 55°

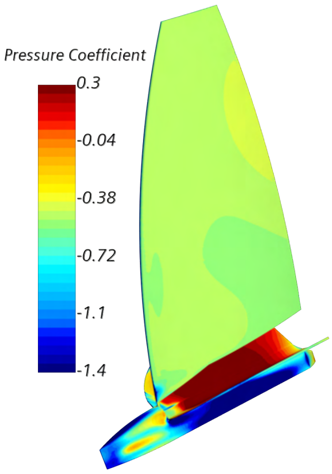

(d) TWA: 75°

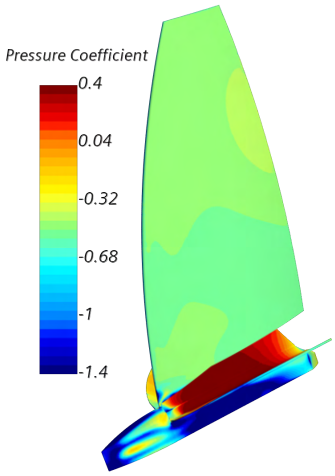

(e) TWA: 110°

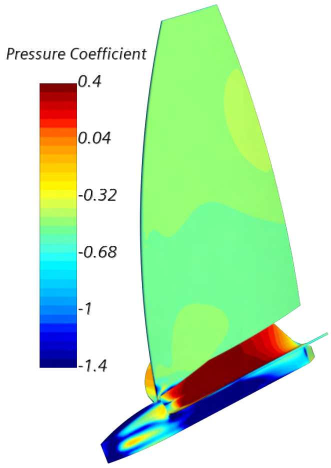

(f) TWA: 120°

Figure B.2: Pressure coefficient leeward side (ISO view, triangular)

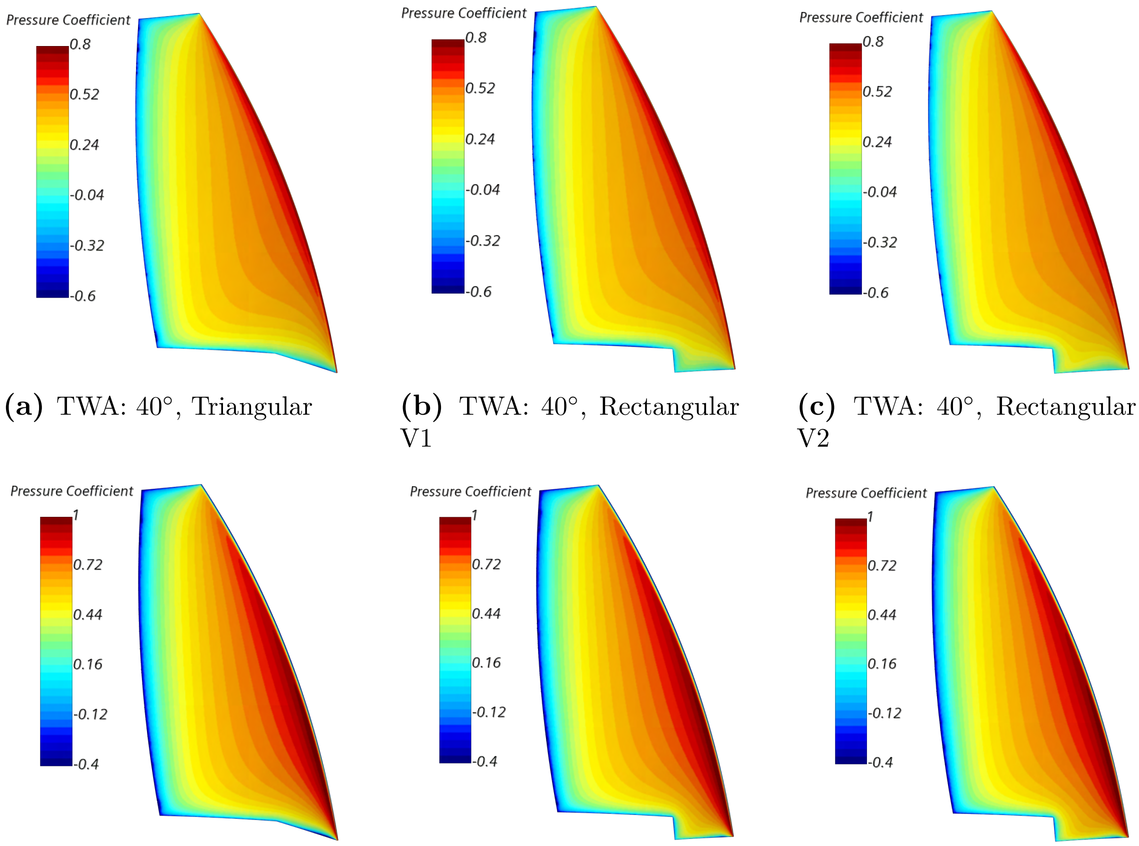

(a) TWA: 40°, Triangular

(b) TWA: 40°, Rectangular V1

(c) TWA: 40°, Rectangular V2

(d) TWA: 120°, Triangular

(e) TWA: 120°, Rectangular V1

(f) TWA: 120°, Rectangular V2

Figure B.3: Pressure coefficient windward side (sail view)

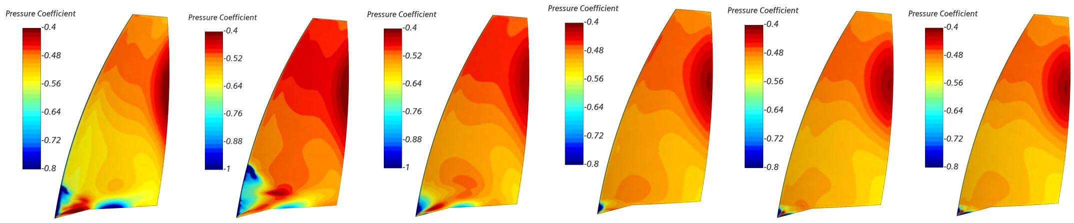

(a) TWA: 40° **(b)** TWA: 45° **(c)** TWA: 55° **(d)** TWA: 75° **(e)** TWA: 110° **(f)** TWA: 120°

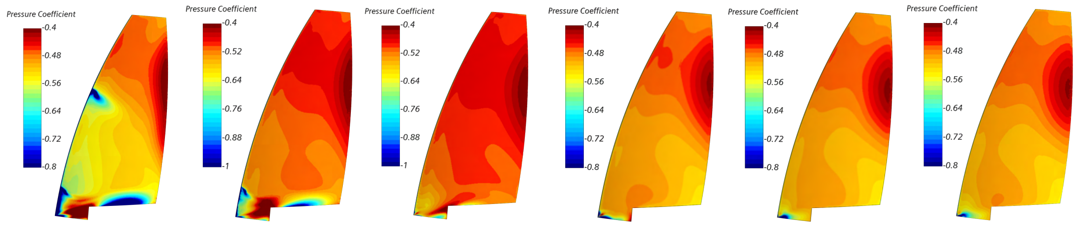

(g) TWA: 40° **(h)** TWA: 45° **(i)** TWA: 55° **(j)** TWA: 75° **(k)** TWA: 110° **(l)** TWA: 120°

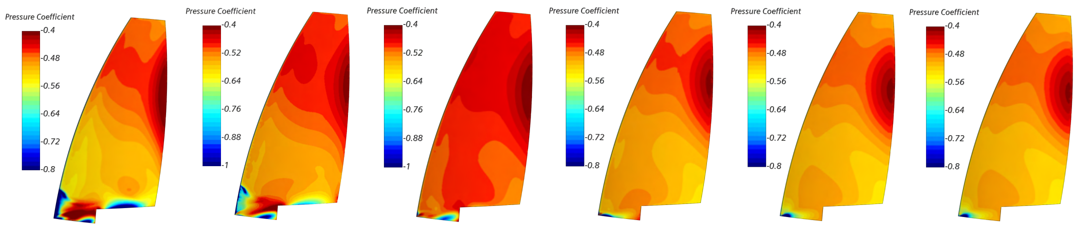

(m) TWA: 40° **(n)** TWA: 45° **(o)** TWA: 55° **(p)** TWA: 75° **(q)** TWA: 110° **(r)** TWA: 120°

Figure B.4: Pressure coefficient leeward side (sail view)

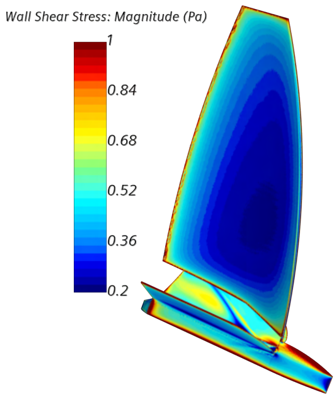

(a) TWA: 40°

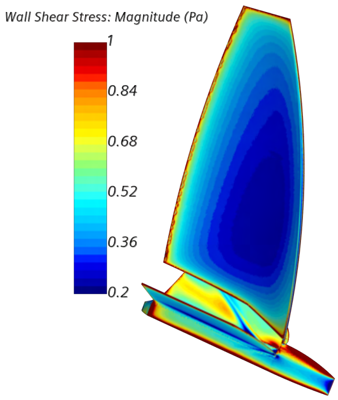

(b) TWA: 45°

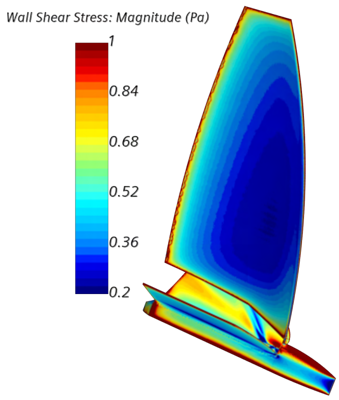

(c) TWA: 55°

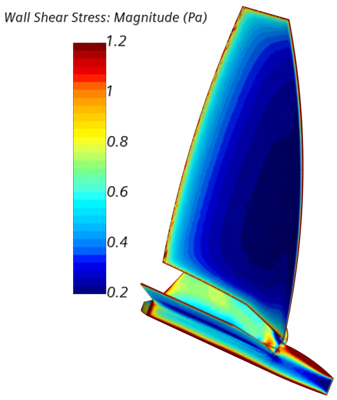

(d) TWA: 75°

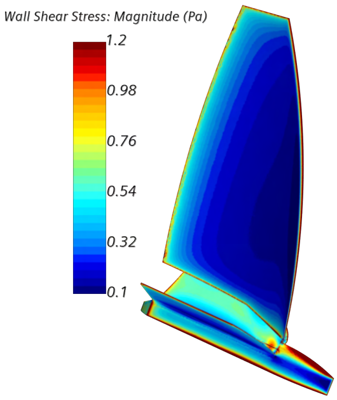

(e) TWA: 110°

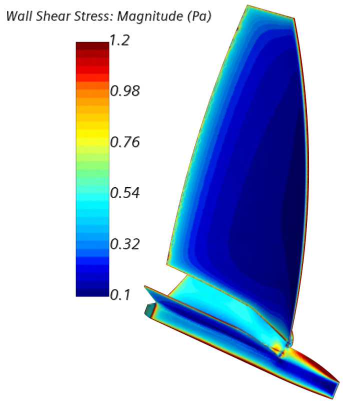

(f) TWA: 120°

Figure B.5: Wall shear stress windward side (ISO view, triangular)

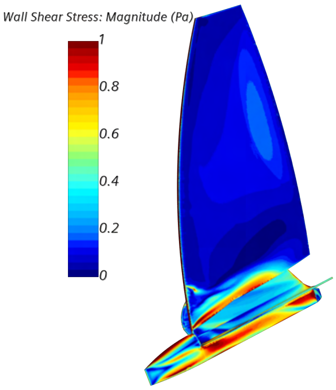

(a) TWA: 40°

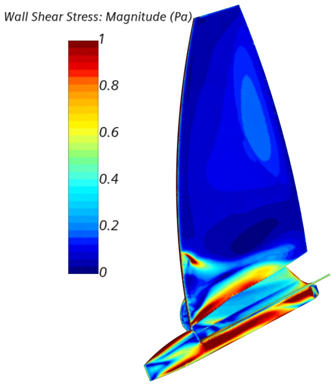

(b) TWA: 45°

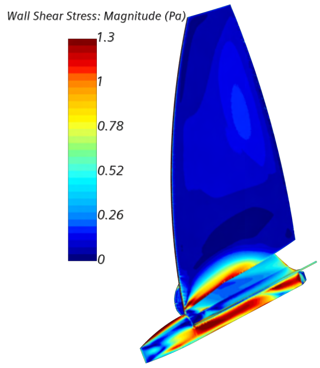

(c) TWA: 55°

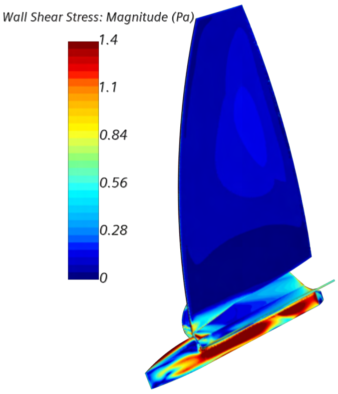

(d) TWA: 75°

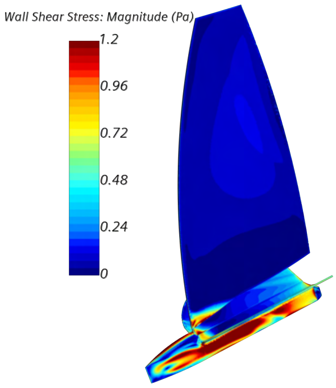

(e) TWA: 110°

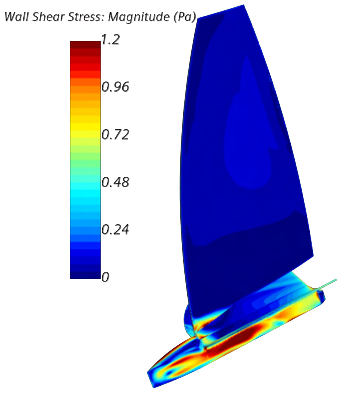

(f) TWA: 120°

Figure B.6: Wall shear stress leeward side (ISO view, triangular)

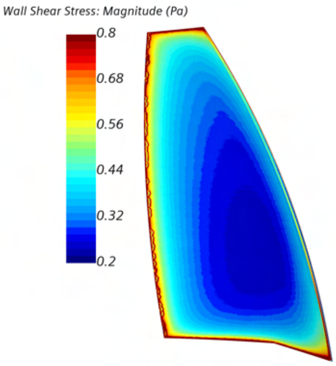

(a) TWA: 40°, Triangular

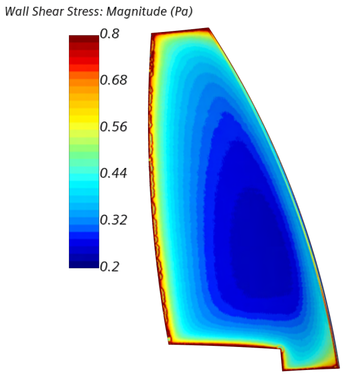

(b) TWA: 40°, Rectangular V1

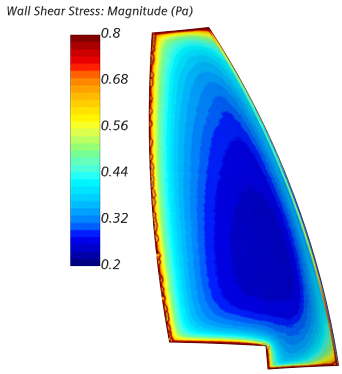

(c) TWA: 40°, Rectangular V2

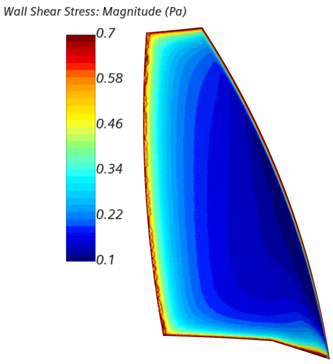

(d) TWA: 120°, Triangular

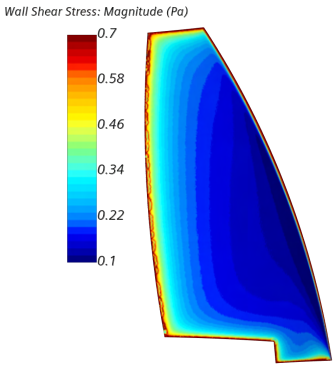

(e) TWA: 120°, Rectangular V1

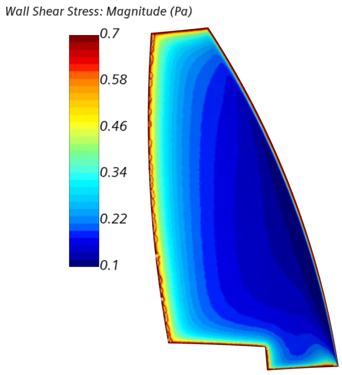

(f) TWA: 120°, Rectangular V2

Figure B.7: Wall shear stress windward side (sail view)

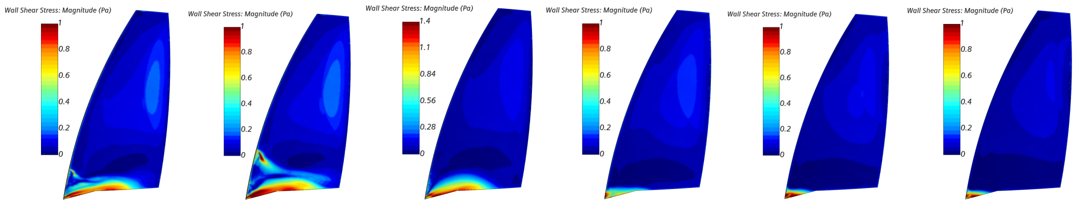

(a) TWA: 40° (b) TWA: 45° (c) TWA: 55° (d) TWA: 75° (e) TWA: 110° (f) TWA: 120°

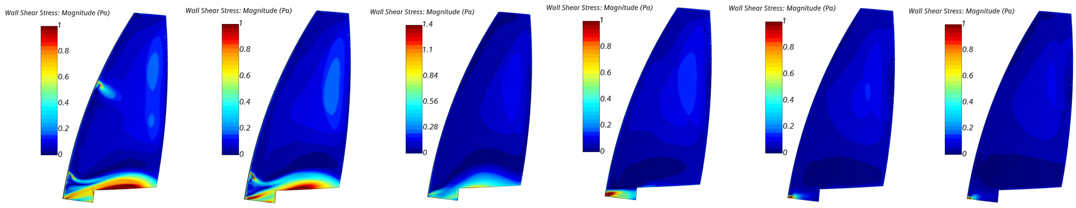

(g) TWA: 40° (h) TWA: 45° (i) TWA: 55° (j) TWA: 75° (k) TWA: 110° (l) TWA: 120°

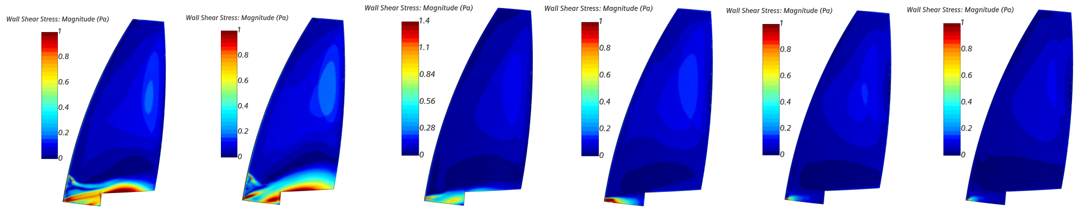

(m) TWA: 40° (n) TWA: 45° (o) TWA: 55° (p) TWA: 75° (q) TWA: 110° (r) TWA: 120°

Figure B.8: Wall shear stress leeward side (sail view)

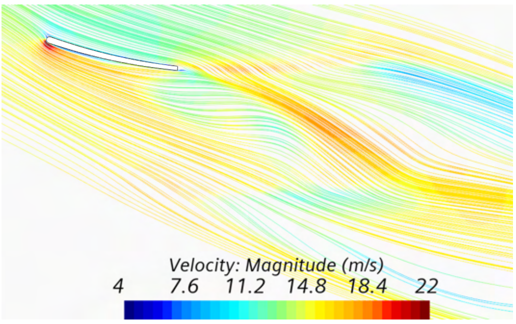

(a) z = 0.75 m

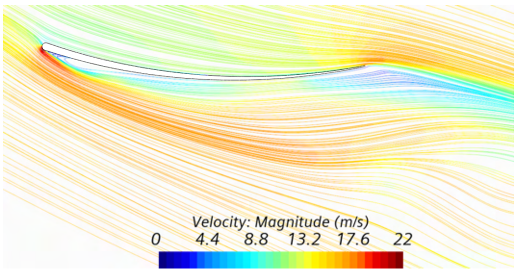

(b) z = 1 m

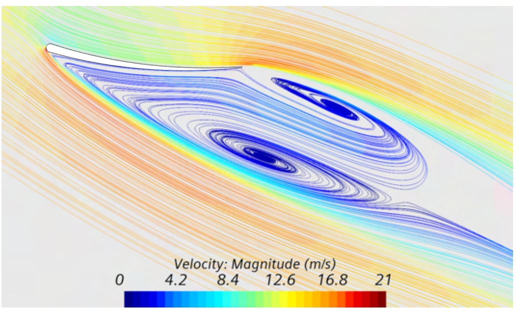

(c) z = 3 m

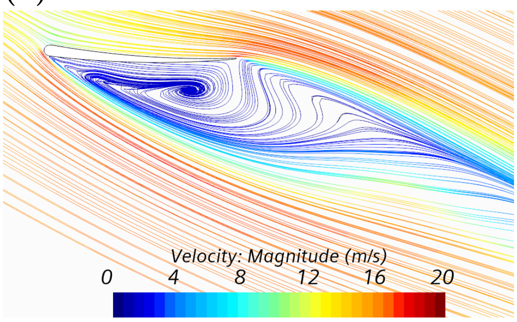

(d) z = 5 m

Figure B.9: Variation in flow along the height of the sail (TWA: 40°)

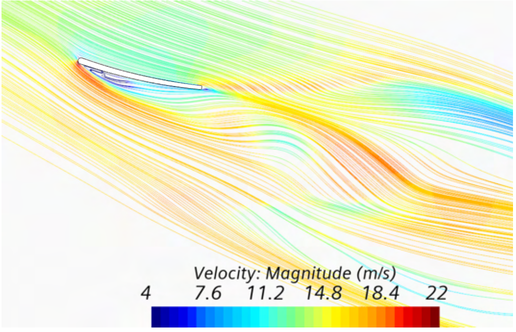

(a) z = 0.75 m

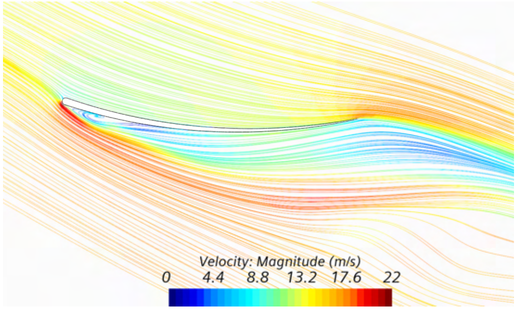

(b) z = 1 m

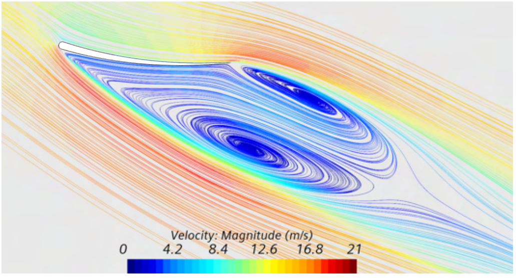

(c) z = 3 m

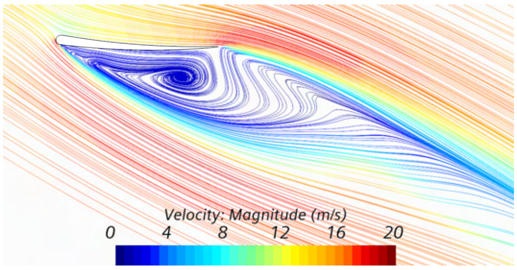

(d) z = 5 m

Figure B.10: Variation in flow along the height of the sail (TWA: 45°)

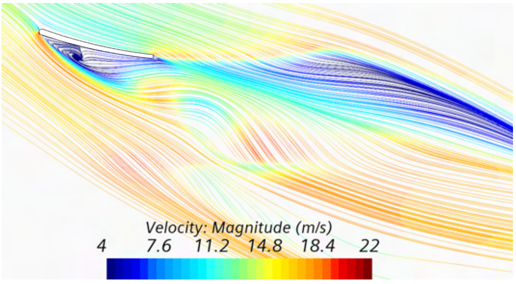

(a) z = 0.75 m

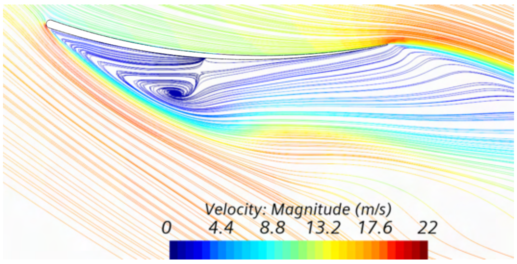

(b) z = 1 m

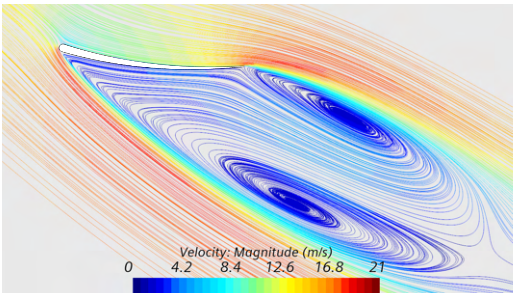

(c) z = 3 m

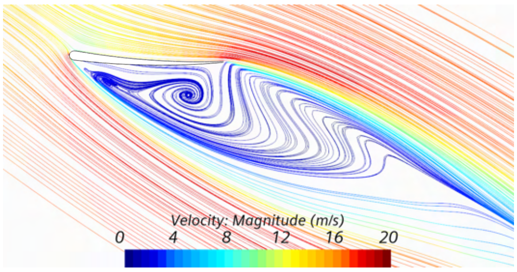

(d) z = 5 m

Figure B.11: Variation in flow along the height of the sail (TWA: 55°)

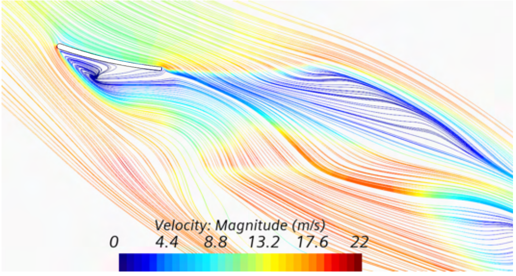

(a) z = 0.75 m

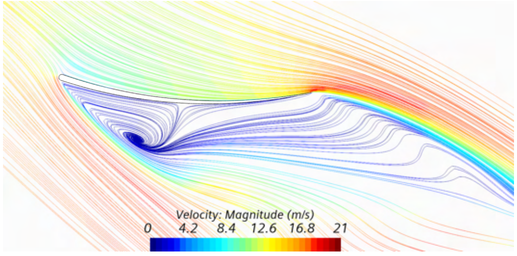

(b) z = 1 m

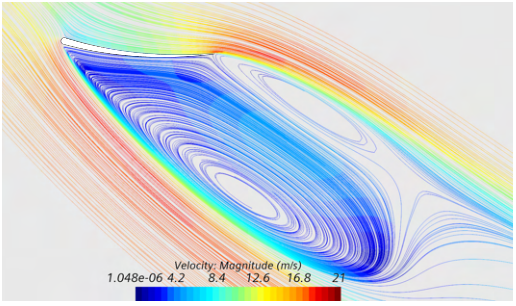

(c) z = 3 m

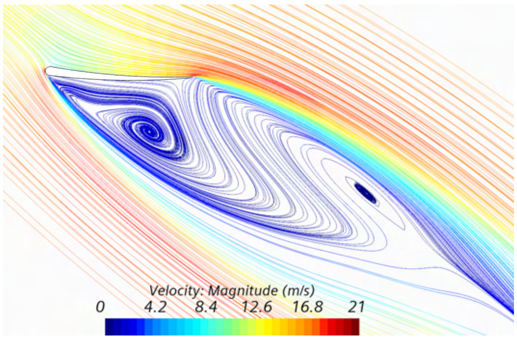

(d) z = 5 m

Figure B.12: Variation in flow along the height of the sail (TWA: 75°)

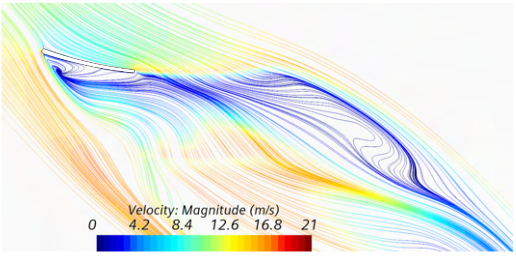

(a) z = 0.75 m

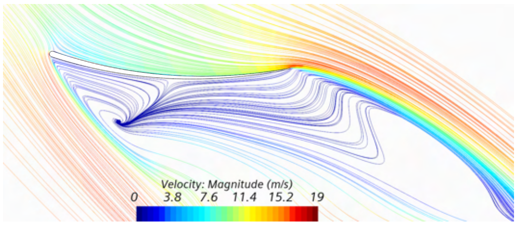

(b) z = 1 m

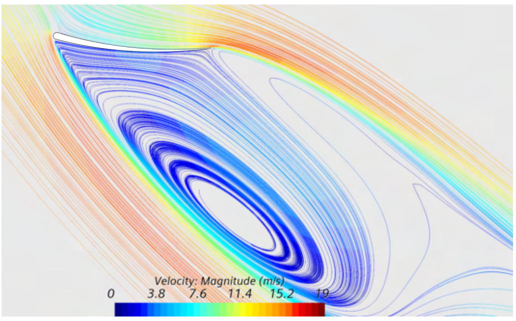

(c) z = 3 m

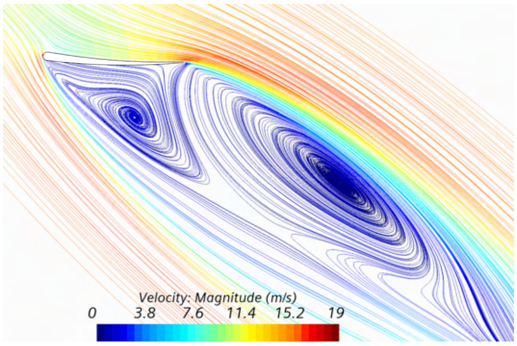

(d) z = 5 m

Figure B.13: Variation in flow along the height of the sail (TWA: 110°)

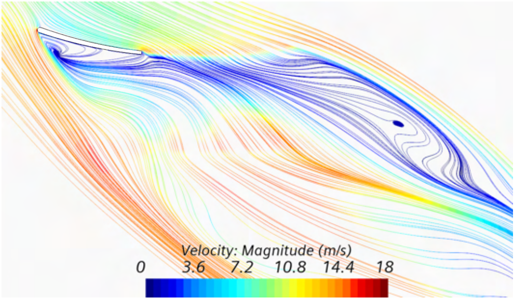

(a) z = 0.75 m

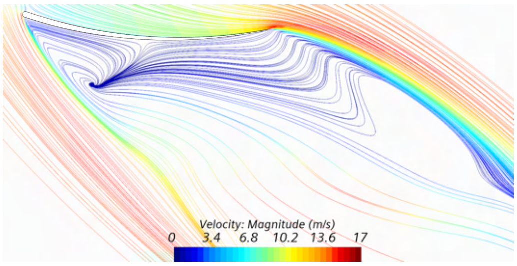

(b) z = 1 m

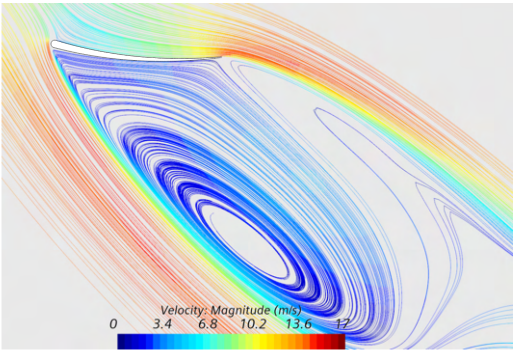

(c) z = 3 m

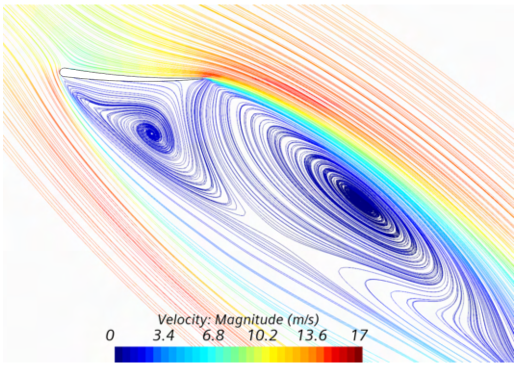

(d) z = 5 m

Figure B.14: Variation in flow along the height of the sail (TWA: 120°)

C
Numerical Results

Table C.1: Lateral forces (y-direction) in N

TWA [°]	**Deck Sweeper**	F_{LAT} **Total**	F_{LAT} **Sail**	F_{LAT} **Hull**	F_{LAT} **Wings**
40	Triangular	-961.6	-827.7	-84.9	-49.0
40	Rectangular V1	-981.5	-849.7	-85.7	-46.1
40	Rectangular V2	-964.4	-834.2	-87.1	-43.1
45	Triangular	-1085.5	-927.0	-100.9	-57.6
45	Rectangular V1	-1077.3	-920.6	-101.0	-55.7
45	Rectangular V2	-1099.8	-947.4	-102.2	-50.2
55	Triangular	-1225.0	-1019.0	-129.0	-77.0
55	Rectangular V1	-1190.2	-989.5	-128.7	-72.0
55	Rectangular V2	-1196.3	-1000.8	-129.1	-66.4
75	Triangular	-1313.6	-1044.6	-166.2	-102.8
75	Rectangular V1	-1318.3	-1058.6	-165.2	-94.5
75	Rectangular V2	-1322.0	-1071.8	-162.0	-88.2
110	Triangular	-1082.7	-853.3	-141.9	-87.5
110	Rectangular V1	-1083.9	-863.2	-141.0	-79.7
110	Rectangular V2	-1091.2	-875.1	-139.5	-76.6
120	Triangular	-912.9	-720.1	-119.1	-73.7
120	Rectangular V1	-915.0	-728.4	-119.3	-67.3
120	Rectangular V2	-922.1	-738.8	-118.5	-64.8

Table C.2: Driving forces (x-direction) in N

TWA [°]	Deck Sweeper	F_R Total	F_R Sail	F_R Hull	F_R Wings
40	Triangular	60.1	70.6	-5.9	-4.6
40	Rectangular V1	65.4	76.1	-6.0	-4.7
40	Rectangular V2	63.3	74.1	-6.0	-4.8
45	Triangular	73.2	83.9	-5.9	-4.8
45	Rectangular V1	70.9	81.6	-5.8	-4.9
45	Rectangular V2	74.4	85.0	-5.8	-4.8
55	Triangular	84.2	93.6	-4.7	-4.7
55	Rectangular V1	82.6	92.9	-5.8	-4.5
55	Rectangular V2	84.1	94.5	-5.8	-4.6
75	Triangular	96.8	103.9	-4.0	-3.1
75	Rectangular V1	100.7	108.6	-4.5	-3.4
75	Rectangular V2	102.3	110.2	-4.5	-3.4
110	Triangular	83.3	87.0	-1.4	-2.3
110	Rectangular V1	86.8	91.1	-1.7	-2.6
110	Rectangular V2	88.3	92.7	-1.8	-2.6
120	Triangular	69.5	73.4	-1.9	-2.0
120	Rectangular V1	72.9	76.9	-1.7	-2.3
120	Rectangular V2	74.5	78.2	-1.5	-2.2

Table C.3: Lifting forces (z-direction) in N

TWA [°]	Deck Sweeper	F_z Total	F_z Sail	F_z Hull	F_z Wings
40	Triangular	-110.1	27.7	-100.2	-37.6
40	Rectangular V1	-100.4	28.3	-99.5	-29.2
40	Rectangular V2	-106.7	27.7	-103.5	-30.9
45	Triangular	-137.2	13.7	-103.5	-47.4
45	Rectangular V1	-135.2	30.8	-121.9	-44.1
45	Rectangular V2	-133.1	32.3	-126.5	-38.9
55	Triangular	-210.7	35.2	-161.3	-84.6
55	Rectangular V1	-211.8	35.9	-165.0	-82.7
55	Rectangular V2	-214.8	36.3	-169.0	-82.1
75	Triangular	-309.5	41.0	-209.2	-141.3
75	Rectangular V1	-299.9	41.5	-210.6	-130.8
75	Rectangular V2	-298.2	42.0	-214.5	-125.7
110	Triangular	-253.1	33.6	-176.1	-110.6
110	Rectangular V1	-239.7	35.2	-174.5	-100.4
110	Rectangular V2	-243.3	35.8	-177.0	-102.1
120	Triangular	-204.5	28.3	-144.1	-88.7
120	Rectangular V1	-197.1	29.9	-145.3	-81.7
120	Rectangular V2	-202.8	30.3	-148.6	-84.5

Table C.4: Moments in Nm (Origin at the hull-mast intersection)

TWA [°]	**Deck Sweeper**	M_x	M_y	M_z
40	Triangular	-41.1	-1793.2	-1302.2
40	Rectangular V1	-58.4	-1810.8	-1317.2
40	Rectangular V2	-45.8	-1760.8	-1289.7
45	Triangular	-34.5	-1993.2	-1455.1
45	Rectangular V1	-35.4	-1972.0	-1444.2
45	Rectangular V2	-45.4	-1990.8	-1471.1
55	Triangular	11.9	-2217.7	-1646.8
55	Rectangular V1	15.8	-2132.6	-1584.3
55	Rectangular V2	14.2	-2125.7	-1591.0
75	Triangular	84.3	-2295.4	-1754.0
75	Rectangular V1	71.9	-2280.8	-1747.7
75	Rectangular V2	65.8	-2278.5	-1751.9
110	Triangular	49.8	-1872.7	-1439.6
110	Rectangular V1	35.8	-1858.4	-1430.6
110	Rectangular V2	40.8	-1861.6	-1440.7
120	Triangular	30.7	-1582.0	-1213.3
120	Rectangular V1	22.9	-1569.5	-1207.5
120	Rectangular V2	30.6	-1572.6	-1216.9

DEPARTMENT OF MECHANICS AND MARITIME SCIENCES
CHALMERS UNIVERSITY OF TECHNOLOGY
Gothenburg, Sweden
www.chalmers.se

CHALMERS
UNIVERSITY OF TECHNOLOGY